Remote Sensing of Environment 216 (2018) 91–104

Contents lists available at ScienceDirect

Remote Sensing of Environment

journal homepage: www.elsevier.com/locate/rse

Estimation of ultrahigh resolution $PM_{2.5}$ concentrations in urban areas using 160 m Gaofen-1 AOD retrievals

Tianhao Zhang[a], Zhongmin Zhu[a,b], Wei Gong[a,c,*], Zerun Zhu[a], Kun Sun[a,**], Lunche Wang[d], Yusi Huang[a], Feiyue Mao[a,c,e], Huanfeng Shen[a,c,f], Zhiwei Li[f], Kai Xu[a]

[a] State Key Laboratory of Information Engineering in Surveying, Mapping and Remote Sensing, Wuhan University, Wuhan 430079, China
[b] College of Information Science and Engineering, Wuchang Shouyi University, Wuhan 430064, China
[c] Collaborative Innovation Center for Geospatial Technology, Wuhan 430079, China
[d] Laboratory of Critical Zone Evolution, School of Earth Sciences, China University of Geosciences, Wuhan 430074, China
[e] School of Remote Sensing and Information Engineering, Wuhan University, Wuhan 430079, China
[f] School of Resource and Environmental Sciences, Wuhan University, Wuhan 430079, China

ARTICLE INFO

Keywords:
Aerosol optical depth
Ultrahigh spatial resolution
Gaofen-1 WFV
Nested LME model
Urban-scale $PM_{2.5}$

ABSTRACT

Satellite-derived aerosol optical depth (AOD) has been widely used to estimate ground-level $PM_{2.5}$ concentrations due to its spatially continuous observation. However, the coarse spatial resolutions (e.g., 3 km, 6 km, or 10 km) of the primary satellite AOD products have weakness to capture the characteristics of urban-scale $PM_{2.5}$ patterns. Moreover, high-resolution (e.g., 1 km) $PM_{2.5}$ estimations are still unable to be related to the urban landscape or to small geographical units, which is crucial for analyzing the urban pollution structure. In this study, the daily $PM_{2.5}$ concentrations were estimated using the new AOD data with a 160 m spatial resolution retrieved by the Gaofen-1 (GF) wide field of view (WFV) along with the nested linear mixed effects model and ancillary variables from the Weather Research & Forecasting (WRF) meteorological simulation data. The experiment was conducted in Wuhan, Beijing, and Shanghai, which suffers from severe atmospheric fine particle pollution in recent years. The proposed model performed well for both GF and Moderate Resolution Imaging Spectroradiometer (MODIS), with slight over-fitting and little spatial autocorrelation. Regarding to the GF $PM_{2.5}$ estimation, model fitting yielded R^2 values of 0.96, 0.91 and 0.95 and mean prediction error (MPE) of 10.13, 11.89 and 7.34 μg/m^3 for Wuhan, Beijing and Shanghai, respectively. The site-based cross validation achieved R^2 values of 0.92, 0.88 and 0.89, and MPE of 13.69, 16.76 and 12.59 μg/m^3 for Wuhan, Beijing and Shanghai, respectively. The day-of-years based cross validation resulted in R^2 of 0.54, 0.58 and 0.50, and MPE of 30.46, 27.12 and 31.58 μg/m^3 for Wuhan, Beijing and Shanghai, respectively, indicating that it was practicable to estimate the GF $PM_{2.5}$ in the days without enough AOD-$PM_{2.5}$ matchups. The ultrahigh resolution $PM_{2.5}$ estimations offer substantial advantages for providing finer spatially resolved $PM_{2.5}$ trends. Additionally, it offers new approaches to locate main $PM_{2.5}$ emission sources, evaluate the local $PM_{2.5}$ contribution proportion, and quantify the daily $PM_{2.5}$ emission level via remote sensing techniques. Along with the joint observations via other high-resolution satellites, the temporal resolution of GF $PM_{2.5}$ will be further improved. In all, this study not only provides possibilities for further applications in the precise analysis of urban inner $PM_{2.5}$ pollution patterns but also establishes a foundation for constructing a high-resolution satellite air monitoring network in China.

1. Introduction

Numerous epidemiological studies have demonstrated that exposure to particulate matter with an aerodynamic diameter of < 2.5 μm ($PM_{2.5}$) is associated with a variety of adverse health effects, including cardiovascular and respiratory diseases, further influencing morbidity and mortality (Beelen et al., 2014; Dockery et al., 1993; Hoek et al., 2013; Pope et al., 2002; Sacks et al., 2011). Population exposure to $PM_{2.5}$ was traditionally conducted by extending ground-level measurements to a certain region, however, this method tended to underestimate health risks due to exposure misclassification (J. Hu et al., 2014; X. Hu et al., 2014; Pinto et al., 2004; Qian et al., 2016).

* Correspondence to: W. Gong, State Key Laboratory of Information Engineering in Surveying, Mapping and Remote Sensing, Wuhan University, Wuhan 430079, China.
** Corresponding author.
E-mail addresses: weigong@whu.edu.cn (W. Gong), sunk@sustc.edu.cn (K. Sun).

https://doi.org/10.1016/j.rse.2018.06.030
Received 21 June 2017; Received in revised form 21 June 2018; Accepted 22 June 2018

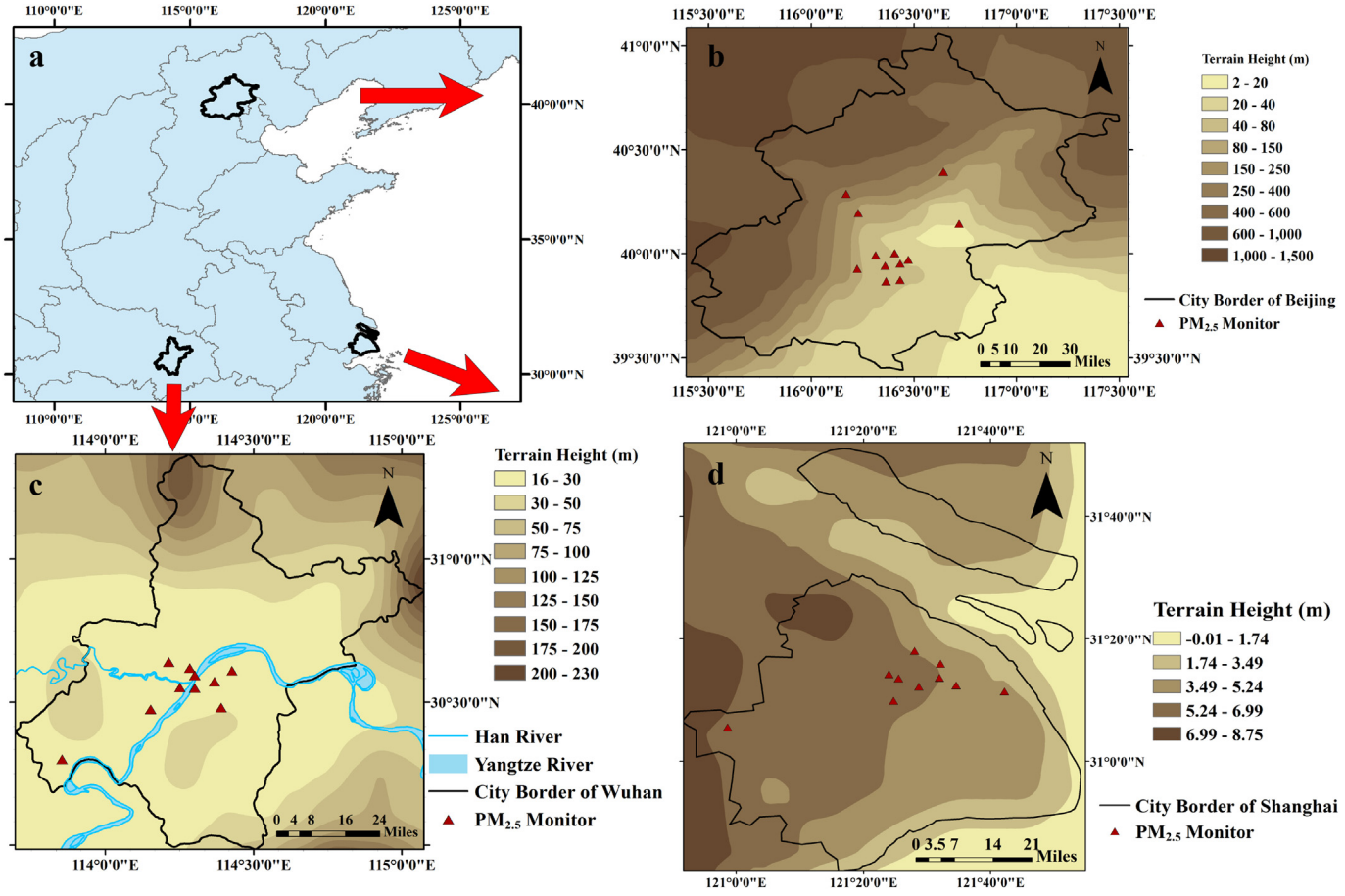

Fig. 1. Study areas with the terrain height and locations of the state-controlled $PM_{2.5}$ monitoring stations.

Therefore, the spatially and temporally continuous estimation of $PM_{2.5}$ is significant for epidemiological research and effective assessments of atmospheric quality (Li et al., 2011; Van et al., 2015).

In contrast to the limited spatial coverage of ground monitoring, satellite remote sensing techniques can provide spatially continuous observations and has therefore been adopted to estimate ambient $PM_{2.5}$ (Che et al., 2014; Gupta et al., 2006; Zhang et al., 2016a). Since the satellite-derived aerosol optical depth (AOD) measures the total light extinction consisting of aerosol absorption and scattering in a specific atmospheric column, AOD is related to the loadings of particular matter in that column to a certain extent (Chu et al., 2003; Engelcox et al., 2004; Zhang et al., 2016b). A series of AOD products derived from satellite sensors, mainly including the Moderate Resolution Imaging Spectroradiometer (MODIS) (Hu et al., 2013a; Liu et al., 2007a; Ma et al., 2016; Zhang et al., 2009), the Visible Infrared Imaging Radiometer Suite (VIIRS) (Oo et al., 2013; Wu et al., 2016), and the Multi-angle Imaging SpectroRadiometer (MISR) (Liu et al., 2007a; Liu et al., 2007b; Liu et al., 2007c) have been adopted in previous studies to estimate ambient $PM_{2.5}$ concentrations. However, the MODIS, VIIRS, and MISR have nominal spatial resolutions for AOD retrieval of 10 km (3 km via dark target algorithm), 6 km (750 m in VIIRS intermediate product), and 17.6 km, respectively, which is generally too coarse for precise exposure estimates in urban areas (Chudnovsky et al., 2014). Along with the development of the Multi-Angle Implementation of Atmospheric Correction (MAIAC) algorithm, which provide MODIS AOD products with 1 km resolution (Lyapustin et al., 2011a; Lyapustin et al., 2011b; Lyapustin et al., 2012), estimations of $PM_{2.5}$ with 1 km resolution have been conducted to investigate the spatial patterns of $PM_{2.5}$ and pollution levels at the urban scale (Chudnovsky et al., 2013; Chudnovsky et al., 2014; J. Hu et al., 2014; X. Hu et al., 2014; Hu et al., 2013b; Qian et al., 2016).

Nevertheless, current studies could only adopt ground-monitored $PM_{2.5}$ to explore the effects of urban landscape patterns on $PM_{2.5}$ (Wu et al., 2015; Zhang et al., 2015), because the current spatial resolution of $PM_{2.5}$ estimation is still too coarse to meet the requirements perfectly for analyzing urban pollution structure or the relationship between the urban landscapes and $PM_{2.5}$ concentrations. Since the distribution of ground-monitoring sites is generally sparse and spatially uneven, the urban analysis based on ground-monitored $PM_{2.5}$ cannot represent integral situations to a certain extent. Therefore, it is necessary to estimate $PM_{2.5}$ concentrations with ultrahigh spatial resolution via high-resolution AOD retrievals, especially in urban areas. Based on our recent study, GaoFen-1 (GF) wide field of view (WFV) was applied to retrieve AOD with a 160 m spatial resolution (Sun et al., 2017); these measurements can then be used to obtain $PM_{2.5}$ estimations at this resolution. Moreover, GF AOD has been demonstrated to cover urban surfaces by correcting the background atmospheric effect and obtaining local aerosol models; these data achieved ideal validation results when compared to ground sun-photometer measurements in central China (Sun et al., 2017). This GF AOD with ultrahigh spatial resolution can provide potential applications in locating emission sources of atmospheric pollutants and can offer new opportunities for exploring $PM_{2.5}$ problem at the district scale, block scale, or even building scale in cities under dense urbanization. In addition, the linear mixed effects (LME) model was first applied in estimating $PM_{2.5}$ concentrations in 2011 (Lee et al., 2011), which was then widely adopted due to its great power in making highly accurate estimates of $PM_{2.5}$ concentrations via remote sensing techniques (Lee et al., 2011; Xie et al., 2015; Ghotbi et al., 2016). Because the original LME model failed to predict $PM_{2.5}$ in the days without $PM_{2.5}$-AOD matchups, the nested linear mixed effects

model was developed to improve the temporal coverage of satellite-derived $PM_{2.5}$ (Ma et al., 2016). Based on the characteristics of the GF revisit period, the day-specific and month-specific nested LME model was developed in this study to estimate GF $PM_{2.5}$ with better temporal coverage.

The primary objective of this study is to evaluate the performance of ground-level $PM_{2.5}$ estimation in three representative cities of China via a nested LME model using 160 m GF AOD combined with three nested Weather Research & Forecasting (WRF) meteorological simulation data as ancillary parameters. The spatial patterns and accuracy of the GF $PM_{2.5}$ estimations were evaluated using model fitting, site-based cross-validation and day-of-years based cross-validation. The advantages of the $PM_{2.5}$ estimation with ultrahigh spatial resolution were then discussed by using current mainstream $PM_{2.5}$ estimations as references. The extra value of GF $PM_{2.5}$ was demonstrated through a case analysis, i.e. potential applications for locating and quantifying the main sources of $PM_{2.5}$ emissions in Wuhan. Finally, the limitations of GF $PM_{2.5}$ were discussed, and future work was accordingly proposed to solve the remaining problems in spatial variation and temporal resolution.

2. Materials and methods

2.1. Study area

The experimental areas in this study focused on three major cities in China, including Wuhan, Beijing, and Shanghai. As illustrated in Fig. 1a and c, Wuhan, which is one of the largest cities in central China, is located at the confluence of the Yangtze River and Han River. Leading the Rise of Central China Plan, Wuhan has gradually become one of the significant pivots in industry, transportation and economy. However, due to the rapid development of urbanization and industrialization, which includes construction, smelting and cement processing, atmospheric pollution problems have become increasingly prominent (Wang et al., 2015; Wang et al., 2013), raising concern from both the government and public (Song et al., 2016). As shown in Fig. 1a and b, Beijing, which is the capital of China, is located in the northern part of the North China Plain. Given the dense industrialization, urbanization and motorization in recent years, particulate pollution, especially $PM_{2.5}$ pollution, has become a problem that demands prompt solution **in** Beijing (Han et al., 2014; J. Hu et al., 2014; X. Hu et al., 2014). As demonstrated in Fig. 1a and d, Shanghai, which is the economic center of China, is located in eastern China. Leading the rapid economic growth and accelerated urbanization in the Yangtze River Delta, Shanghai also suffers from severe air quality problems from $PM_{2.5}$ pollution in recent years (J. Hu et al., 2014; X. Hu et al., 2014; Qiao et al., 2016).

2.2. $PM_{2.5}$ measurements

The national air quality monitoring network in China has been established by the Chinese Ministry of Environmental Protection (MEP) since 2013. The hourly datasets of the mass concentration of $PM_{2.5}$, which are measured using the tapered element oscillating microbalance (TEOM) method or β-attenuation monitors, can be downloaded from the website of the China Environmental Monitoring Center (http://113.108.142.147:20035/emcpublish/). Fig. 1 shows the locations of monitoring stations in three cities that measured the hourly $PM_{2.5}$ data for the experimental period from 2014 to 2015. Since the GF-1 WFV passed over equator at approximately 10:30 a.m. local time, the averaged $PM_{2.5}$ of the measured $PM_{2.5}$ at 10:00 a.m. and 11:00 a.m. was adopted in modeling to correspond to the GF AOD.

2.3. Satellite data

2.3.1. GF-1 WFV-derived AOD and validation

The GaoFen-1 was the first satellite of the civilian High-Definition Earth Observation Satellite (HDEOS) project in China and was launched in April 2013. This satellite has four integrated WFV cameras possessing four multi-spectral bands, spanning from the visible to the near-infrared region, with a 16 m spatial resolution. The swath width of the four combined WFV reached to 800 km, which theoretically achieves a temporal resolution of four days, which is better than that of other high spatial resolution satellites (such as Landsat of 16-day temporal resolution), providing the capability for atmospheric observation and monitoring at large scales (Li et al., 2017). The GF imagery data were resampled to a 16 m spatial resolution after homogenized radiation calibration and systematic geometric correction on four WFV cameras, and these data were adopted for AOD retrieval in this study. The preprocesses primarily consisted of precise geometric correction, radiometric calibration, gaseous absorption correction, and cloud mask. The precise geometric correction ensured accuracy within 2 pixels, and radiometric cross-calibration was conducted using Operational Land Imager (OLI) data from Landsat 8, especially for the WFV cameras without onboard calibration (Feng et al., 2016). GF AOD was simulated based on the establishment of look-up-table (LUT) via the 6S radiative transfer model with local aerosol types and build of surface reflectance database (Sun et al., 2017). Because using an inappropriate aerosol model has been demonstrated to influence the accuracy of AOD retrieval (Li et al., 2007), the local aerosol model used for GF AOD retrieval in this study was obtained from long-term sun-photometer observations due to complex aerosol optical properties in Wuhan (Wang et al., 2015). Another key point in GF AOD retrieval is determination of the surface reflectance, as a higher spatial resolution would result in a more complex surface reflectivity. The clear sky composite technique, which is widely used in the MODIS deep blue (DB) algorithm (Levy et al., 2013) and in the high-resolution AOD retrieval from MODIS and Landsat (Luo et al., 2015; Man et al., 2011), was used for GF AOD retrieval allowing for its relatively high temporal and spatial resolution. This method was improved on identification of the clearest days, and correction of the background atmospheric effect was applied at a 10×10 window scale (corresponding to 160 m spatial resolution). In addition to that, our latest studies about geometrical calibration (Zhang et al., 2017) and cloud detection (Li et al., 2017) for GF-1 WFV contributed to the GF-1 AOD retrievals in Beijing and Shanghai.

Moreover, the validation between GF-derived AOD and ground-observed AOD was conducted to ensure the credibility of GF AOD, and the detailed collocation criterion and the validation results were described in our previous research (Sun et al., 2017) and supporting information (SI, Text S1, Fig. S1, and Fig. S2). Good relationships were shown between the GF AOD and ground measurements, with coefficients of determination (R^2) of 0.80, 0.77, and 0.71 in Wuhan, Beijing, and Shanghai, respectively. In addition, validation against the operational MODIS Collection 6 (C6) DB AOD with 10 km spatial resolution showed reasonable relationships, with R^2 values of 0.66, 0.70, and 0.75, respectively (SI, Text S1, Fig. S3, and Fig. S4). In this study, all the validated GF AOD data from January 2014 to December 2015 were applied into model construction by filtering out the AOD values adjacent to clouds because of the unreliable AOD retrieval at cloud edges (Just et al., 2015).

2.3.2. MODIS-derived AOD

For comparison and reference, the Terra DB AOD products with a 10 km spatial resolution were adopted in this study. These products were selected because the GF-1 satellite, which was designed with sun synchronous recurrent orbit, crosses the equator at approximately the same time as Terra (approximately 10:30 a.m. local time). Moreover, the GF AOD retrieval algorithm was similar to the MODIS DB AOD retrieval algorithm. The Level 2 aerosol products from MODIS C6 were downloaded from National Aeronautics and Space Administration (NASA) Level 1 and Atmosphere Archive and Distribution System (LAADS) (http://ladsweb.nascom.nasa.gov/) for 2014–2015, and only those AOD retrievals that achieved the required quality assurance (QA)

flag were used (QA flag = 2 or 3 for DB AOD) to ensure the accuracy of the coefficient estimation in the nested LME model (Ma et al., 2016; Song et al., 2014).

2.3.3. MODIS-derived vegetation index

The Normalized Difference Vegetation Index (NDVI) and Enhanced Vegetation Index (EVI) are vegetation indexes that represent vegetation biomass (Huete et al., 2002). The Terra-MODIS NDVI datasets and Terra-MODIS EVI datasets, with a spatial resolution of 250 m × 250 m and a temporal resolution of 16 days (MOD13Q1), were obtained from NASA LAADS (http://ladsweb.nascom.nasa.gov/) during the experimental period.

2.4. Meteorological data

The hourly meteorological parameters with a 3 km spatial resolution were derived from the WRF model. WRF is a new-generation mesoscale numerical weather prediction system that offers both meteorological applications and operational forecasts (http://www.wrf-model.org/index.php) (Bai et al., 2016; Zheng et al., 2015; Zheng et al., 2016). In this study, the WRF Processing System (WPS) v3.6 was used to generate the initial and boundary conditions based on the three nested domain using the National Centers for Environmental Prediction Final Analysis (NCEP-FNL) reanalysis datasets (http://cfs.ncep.noaa.gov/). WRF v3.4.1 was then employed to drive a one-way nested simulation with resolutions of 27 km, 9 km, and 3 km. The selection of physical options for the WRF simulation mainly included the single-moment 6-class (WSM6) microphysics, the rapid radiative transfer model (RRTM) longwave radiation scheme, the Dudhia shortwave radiation scheme, the Monin-Obukhov surface-layer scheme, the Noah land surface model, the Yonsei University (YSU) planetary boundary layer model, and the Kain-Fritsch cumulus parameterization scheme. The wind speed lag used in this study was the summation of hourly wind speed at 10 m above the ground in the last 24 h. The other meteorological parameters adopted in this study were averaged parameters at 10:00 a.m. and 11:00 a.m., when the Gaofen-1 satellite passed over experimental regions (i.e., approximately 10:30 a.m. local time). Validation of the modeled meteorological parameters was conducted and discussed in detail based on datasets from the National Climate Data Center (NCDC) in SI (Text S2, Table S1, Table S2, and Table S3).

2.5. Data integration

In this study, data integration was performed to ensure that different categories of parameters were spatially consistent before being included in the model. The WRF simulated data under Lambert projection and Terra-MODIS vegetation index datasets were first reprojected into the World Geodetic System 1984 (WGS84) geographic coordinate system and were then resampled using bilinear interpolation to match the AOD grids. Moreover, the AOD values, NDVI/EVI values, and WRF meteorological parameters were both extracted by averaging 3 × 3 pixels centered on the grid where the monitoring stations were located. From the temporal perspective, all the parameters except the wind speed lag were integrated to the average of values at 10:00 a.m. and 11:00 a.m. local time to correspond to the period that GF passed over equator.

2.6. Model structure and validation

In order to develop a reasonable LME model structure, the stepwise selection of auxiliary variables was conducted, following the principle to yield the statistical significance of each variable at the 0.05 level, maximize the model accuracy (R^2), and minimize the Akaike information criterion (AIC). In addition, the fixed and random effects settings, as well as the site-effect parameters for spatial adjustment (Lee et al., 2011; Xie et al., 2015), were also determined by stepwise selection. The detailed selection procedures in Wuhan, Beijing, and Shanghai were described in SI (Text S3, Table S4, Table S5, and Table S6).

The classic LME model is widely acknowledged to be applied in estimating high-accuracy $PM_{2.5}$ using satellite-derived AOD, however, it fails to predict $PM_{2.5}$ concentrations in the days without AOD-$PM_{2.5}$ matchups. A nested LME model with month-, week-, and day-specific random effects was accordingly proposed to abate this deficiency (Ma et al., 2016). Since the temporal resolution of Gaofen-1 WFV is relatively low, the nested LME model can help make use of nearly every valid GF AOD image. Nevertheless, considering the revisiting period of GF WFV and cloud obscuration, there hardly existed over two days, which possessed adequate AOD-$PM_{2.5}$ matchups, in one week. Therefore, we developed a day-month nested LME model instead of the day-week-month nested LME model in previous research, as the model redundancy would be brought by day-week-month nested LME when estimating $PM_{2.5}$ based on GF AOD. The final LME model structure used in Wuhan, Beijing, and Shanghai can be expressed as Eq. (1), Eq. (2), and Eq. (3), respectively.

$$\begin{aligned} PM_{2.5,st} = {} & [b_0 + (b_{0,t,Month}, b_{0,t,Day})] + [b_1 + (b_{1,t,Month}, b_{1,t,Day})] \times AOD_{st} \\ & + [b_2 + (b_{2,t,Month}, b_{2,t,Day})] \times WS10Lag_{st} \\ & + b_3 \times SH2_{st} + b_4 \times PBLH_{st} + s_i + \varepsilon_t (b_{0,t} b_{1,t} b_{2,t}) \sim N[(0,0,0), \Psi] \end{aligned} \quad (1)$$

$$\begin{aligned} PM_{2.5,st} = {} & [b_0 + (b_{0,t,Month}, b_{0,t,Day})] + [b_1 + (b_{1,t,Month}, b_{1,t,Day})] \times AOD_{st} \\ & + [b_5 + (b_{5,t,Month}, b_{5,t,Day})] \times EVI_{st} \\ & + b_6 \times WS10Lag_{st} + s_i + \varepsilon_t (b_{0,t} b_{1,t} b_{5,t}) \sim N[(0,0,0), \Psi] \end{aligned} \quad (2)$$

$$\begin{aligned} PM_{2.5,st} = {} & [b_0 + (b_{0,t,Month}, b_{0,t,Day})] + [b_1 + (b_{1,t,Month}, b_{1,t,Day})] \times AOD_{st} \\ & + b_7 \times T2_{st} + b_8 \times WS10Lag_{st} + s_i + \varepsilon_t (b_{0,t} b_{1,t}) \sim N[(0,0), \Psi] \end{aligned} \quad (3)$$

where $PM_{2.5,\ st}$ is the mass concentration of the $PM_{2.5}$ measurements ($\mu g/m^3$) from the monitoring station at location s in the day of years (DOY) t at the time period in which the GF satellite passed over; b_0 is the fixed intercept; ($b_{0,\ t,\ Month}$, $b_{0,\ t,\ Day}$) are nested random intercepts that include the linear regression intercepts for each month ($b_{0,\ t,\ Month}$) and each day ($b_{0,\ t,\ Day}$) via available matchups in the experimental period; AOD_{st} is the GF-WFV/Terra-MODIS AOD value (unitless) at location s on DOY t; $WS10Lag_{st}$ is the summation of the wind speed (m/s) in the last 24 h from the time period in which the GF satellite passed over at location s on DOY t; $SH2_{st}$ and $PBLH_{st}$ are the specific humidity (SH) (g/kg) and planetary boundary layer height (PBLH) (km) at location s on DOY t at the time period in which GF satellite passed over, respectively; b_1, b_2, b_3, and b_4 are the fixed slopes for AOD, wind speed, SH, and PBLH, respectively; ($b_{1,\ t,\ Month}$, $b_{1,\ t,\ Day}$), ($b_{2,\ t,\ Month}$, $b_{2,\ t,\ Day}$), and ($b_{5,\ t,\ Month}$, $b_{5,\ t,\ Day}$) are nested random slopes for AOD, WS10Lag, and EVI, respectively, which include the linear regression slopes for each month and each day via the available matchups in the experimental period; $s_i \sim N(0, \sigma_s^2)$ is the random intercept term representing the site-effect at location s; and Ψ is the variance–covariance matrix of the day-specific and month-specific random effects. The fixed effects on the slopes of AOD, wind speed, SH, PBLH, EVI, and temperature accounted for the average effects on the $PM_{2.5}$ during the entire experimental period, while the random effects on slopes of AOD, wind speed, and EVI represented the daily variability or monthly variability in their relationships with $PM_{2.5}$. In addition, the site-effect term was interpolated spatially onto each pixel when predicting $PM_{2.5}$ map, based on inverse distance weighted (IDW).

To evaluate the performance of the nested LME model, several statistical indicators, including the R^2, the mean prediction error (MPE) and the square root of the mean squared prediction errors (RMSPE), were calculated between the estimated $PM_{2.5}$ against the ground-level monitoring $PM_{2.5}$. The formulas for MPE and RMSPE are shown as follows:

$$\mathrm{MPE} = \frac{1}{N}\sum_{t=1}^{N} |predicted_t - measured_t| \quad (4)$$

$$\mathrm{RMSPE} = \sqrt{\frac{1}{N}\sum_{t=1}^{N} (predicted_t - measured_t)^2} \quad (5)$$

The N represents the number of predicted-measured $PM_{2.5}$ pairs. The MPE measures the average deviation between predicted values and measured values, and the RMSPE further indicates the degree of dispersion in deviations, which could testify as to whether there existed large deviations in $PM_{2.5}$ estimations. Additionally, the leave-one-out cross validation (LOOCV) (Kohavi, 2001) approach was adopted to examine for potential over-fitting situations, in which the model might perform better on part of the data adopted to fit the model than on untrained data (J. Hu et al., 2014; X. Hu et al., 2014). Since the size of datasets applied into modeling was relatively small, the LOOCV method was conducted based on the monitoring station level (site-based CV) instead of the entire samples (sample-based CV). Each monitoring station was withheld in turn, and the predictors were accordingly estimated by exactly refitting the LME model 12 times in Beijing and 10 times in Wuhan and Shanghai. Since the absolute minimum number of matched observations requited to solve an intercept and a slope is two, it should be mentioned that at least three observations per day were required in this study to improve overall model performance (J. Hu et al., 2014; X. Hu et al., 2014, Wu et al., 2016). Under this condition, nearly 21%, 16%, and 32% of days respectively in Wuhan, Beijing, and Shanghai were removed in the modeling. In addition to that, since the datasets for modeling and validation generally had the same days, the site-based CV cannot be adopted to evaluate the model performances in those days without $PM_{2.5}$-AOD matchups. Therefore, learning from previous studies (Chang et al., 2013; Ma et al., 2016), we also adopted a DOY-based cross validation (DOY-based CV) to assess the accuracy of model prediction in those days beyond the modeling days. In this case, because there were less than ten days that had $PM_{2.5}$-AOD matchups in one month, the days with $PM_{2.5}$-AOD matchups in each month were randomly divided into two subsets. Then, each subset was withheld in turn, and the predictors were accordingly estimated by the nested LME model using the other subset.

3. Results

3.1. Descriptive statistics

The descriptive statistics of the dependent variable and independent variables used in the nested LME model are illustrated in Table 1, including the mean, maximum (Max), minimum (Min), and standard deviation (Std.Dev.) for these variables. Overall, the maximum $PM_{2.5}$ concentrations in Wuhan, Beijing, and Shanghai during the experimental period reached up to 353.50 μg/m^3, 338.00 μg/m^3, and 345.00 μg/m^3, respectively. In addition, the average $PM_{2.5}$ concentrations during the experimental period respectively reached up to 95.66 μg/m^3, 90.44 μg/m^3, and 73.84 μg/m^3, which was respectively 173%, 158%, and 111% greater than the Level 1 of the World Health Organization Air Quality Interim Target (WHO-IT1: 35 μg/m^3) (WHO, 2006). According to the Chinese standard of ambient air quality (China, M. E. P., 2012), approximately 55.8%, 30.1%, and 39.9% of daily $PM_{2.5}$ concentrations exceeded the allowable standard (75 μg/m^3) in Wuhan, Beijing, and Shanghai, respectively. Thus, it was demonstrated that these three cities all suffered from severe fine particle pollution during this period.

Table 1
Descriptive statistics of the dependent variable and independent variables used in the nested LME model.

		Mean	Max	Min	Std. dev.
Wuhan	$PM_{2.5}$ (μg/m^3)	95.66	353.50	4.00	63.99
	AOD (unitless)	0.96	4.26	0.11	0.69
	WS10Lag (m/s)	2.68	5.70	0.79	1.01
	Specific Humidity (g/kg)	7.45	20.78	1.51	5.36
	PBLH (km)	0.51	1.29	0.07	0.24
Beijing	$PM_{2.5}$ (μg/m^3)	90.44	338.00	6.00	57.65
	AOD (unitless)	0.46	3.79	0.10	0.33
	EVI (unitless)	0.15	0.74	0.01	0.13
	WS10Lag (m/s)	2.15	7.37	0.17	1.29
Shanghai	$PM_{2.5}$ (μg/m^3)	73.84	245.00	6.50	49.49
	AOD (unitless)	0.71	3.05	0.01	0.42
	Temperature (K)	286.90	302.64	273.26	8.29
	WS10Lag (m/s)	2.67	6.68	0.39	1.15

Table 2
Fixed slopes of each independent variable in the nested LME model with GF AOD and MODIS DB AOD.

		GF		MODIS DB	
		b_i	P-value	b_i	P-value
Wuhan	Intercept	109.96	< 0.001	112.42	< 0.001
	AOD	25.46	< 0.001	26.08	< 0.001
	Wind speed lag	−6.23	< 0.001	−7.47	< 0.001
	SH	−5.10	< 0.001	−4.13	< 0.001
	PBLH	−2.75	< 0.05	−5.86	< 0.05
Beijing	Intercept	45.12	< 0.001	42.39	< 0.001
	AOD	50.53	< 0.001	51.15	< 0.001
	EVI	−28.56	< 0.001	−13.34	< 0.001
	Wind speed lag	−1.39	< 0.01	−1.53	< 0.01
Shanghai	Intercept	94.92	< 0.001	98.51	< 0.001
	AOD	37.24	< 0.001	40.31	< 0.001
	Temperature	−0.12	< 0.001	−0.15	< 0.001
	Wind speed lag	−4.70	< 0.01	−3.92	< 0.01

3.2. Results of the model fitting and validation

The fixed slopes of each independent variable in the nested LME model fitting with GF AOD are presented in Table 2. For comparison, the fixed slopes of each independent variable in the similar LME model with MODIS DB AOD were estimated, as shown in Table 2. The matched data in days with both GF AOD and MODIS DB AOD available was used in this study for rigorous comparison strategy, and there were 60, 76, and 50 days of datasets in total for modeling during the experimental period in Wuhan, Beijing, and Shanghai, respectively. The intercept and slope of each variable in the nested LME model with GF AOD and MODIS DB AOD were statistically significant at the $\alpha = 0.05$ level. In Wuhan, AOD had a positive relationship with the $PM_{2.5}$ concentrations, while the wind speed, SH, and PBLH had negative relationships with the $PM_{2.5}$ concentrations. In Beijing, AOD had a positive relationship with the $PM_{2.5}$ concentrations, while the EVI and wind speed had negative relationships with the $PM_{2.5}$ concentrations. In Shanghai, AOD had a positive relationship with the $PM_{2.5}$ concentrations, while the temperature and wind speed had negative relationships with the $PM_{2.5}$ concentrations. Whether the relationship was positive or negative primarily depended on their influence on the $PM_{2.5}$ concentration. Since AOD is positively related to the amount of atmospheric particles, a higher AOD level represents a higher $PM_{2.5}$ concentrations as $PM_{2.5}$ accounts for a certain proportion of particles in the air (Wu et al., 2016). The wind speed was negatively correlated with the ground-level $PM_{2.5}$ concentrations, indicating that the dilution effect of wind for atmospheric particles predominated (Liu et al., 2007a; Zhang et al., 2016c). A higher PBLH can not only expand the near-surface atmosphere but also facilitate vertical convection; thus, the PBLH had a negative relationship with the ground-level $PM_{2.5}$. Since the measurements of the $PM_{2.5}$ concentrations represent only dry particles (Liu et al., 2005), more water vapor would lead to lower $PM_{2.5}$ measurements when the AOD value remains constant (Lin et al., 2015). Therefore, SH, which characterizes the mass proportion of water vapor

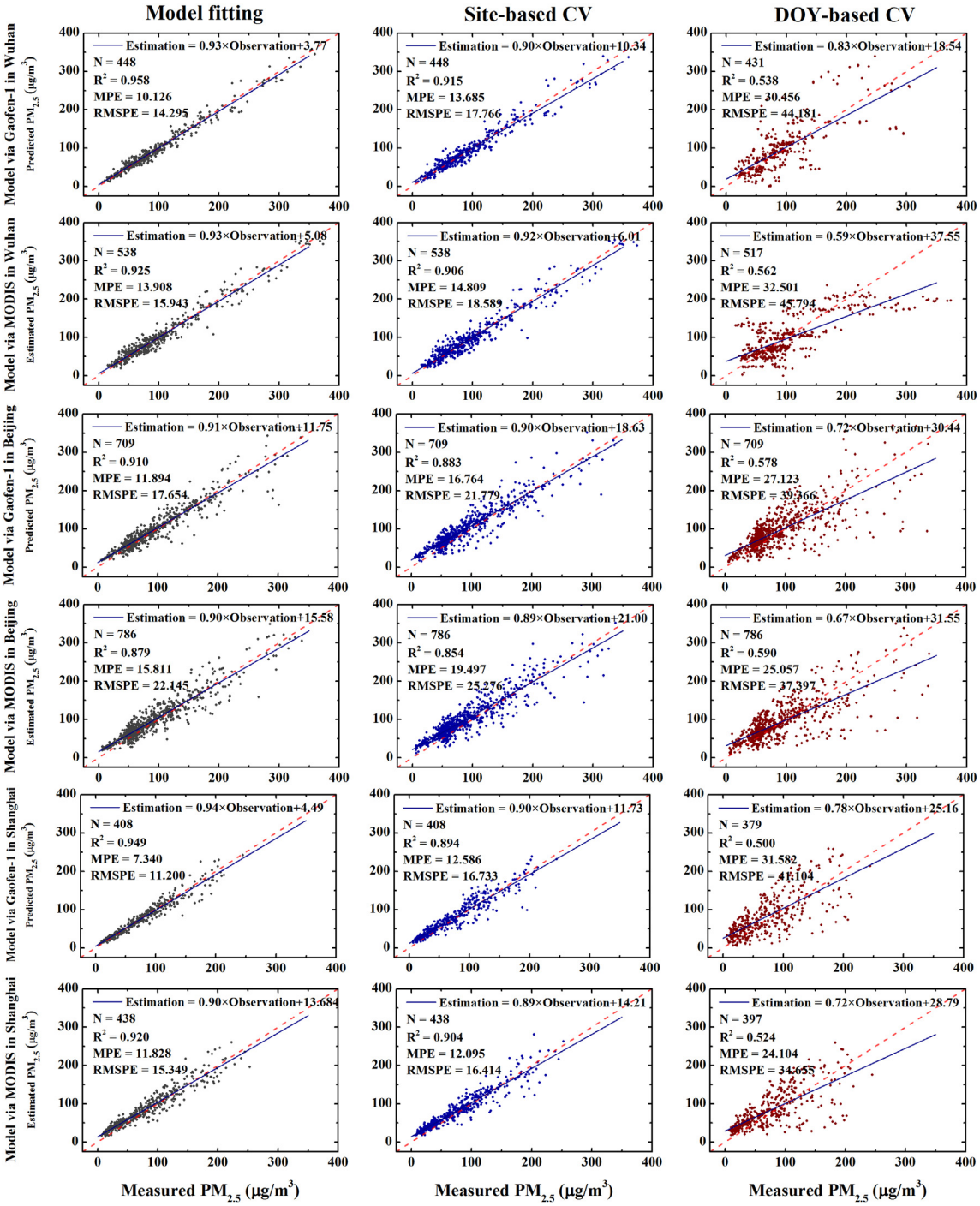

Fig. 2. Model fitting, site-based cross validation, and DOY-based cross validation of the estimated $PM_{2.5}$ against the measured $PM_{2.5}$ in Wuhan, Beijing, and Shanghai. The dashed red lines are the 1:1 reference lines. (For interpretation of the references to color in this figure legend, the reader is referred to the web version of this article.)

in the atmosphere, played a negative role in the increase of ground-level $PM_{2.5}$. The EVI, representing the vegetation variation, can reflect the extent of capturing particulate matters in leaf wax or on plant leaf surfaces (Nowak et al., 2006; Pugh et al., 2012), which possessed a negative role in $PM_{2.5}$ estimation. The temperature in Shanghai had a negative relationship with the ground-level $PM_{2.5}$, which indicated that the negative role such as volatilization of ammonium nitrate at higher temperature (Dawson et al., 2007) was dominant, while the positive role such as higher temperature accelerating the generation of secondary particles (Liu et al., 2007a; Tai et al., 2010) was overwhelmed in Shanghai.

Linear regression was conducted to fit the estimated $PM_{2.5}$ concentrations to the measured $PM_{2.5}$ concentrations, combined with the calculation of R^2, MPE, and RMSPE for model fitting, site-based CV, and DOY-based CV, respectively. As shown in Fig. 2, the R^2 values for the GF model fitting in Wuhan, Beijing, and Shanghai reached up to 0.958, 0.910, and 0.949, respectively. The R^2 values for GF site-based CV in these three cities were relatively high, achieving 0.915, 0.883, and 0.894, respectively. The MPE and RMSPE of GF model fitting and GF site-based CV in these three cities were relatively low. Thus, it was indicated that the $PM_{2.5}$ retrieved by GF AOD agreed well with the ground-level $PM_{2.5}$ measurements. As reference, the model fitting and

cross validation for MODIS DB represented the $PM_{2.5}$ estimated by MODIS DB AOD showed good consistency with the ground-level $PM_{2.5}$ measurements, with R^2 values of 0.925 and 0.906 in Wuhan, 0.879 and 0.854 in Beijing, and 0.920 and 0.904 in Shanghai, respectively. Moreover, a certain extent of model over-fitting occurred in both satellites in three cities. From model fitting to site-based CV, there existed over-fitting situations for both the GF model and MODIS DB model in Wuhan, with R^2 decreasing by 0.043 and 0.019, MPE increasing by 3.559 and 2.836 μg/m^3, and RMSPE increasing by 3.471 and 2.646 μg/m^3, respectively. Similarly, R^2 decreased by 0.027 and 0.025, MPE increased by 4.87 and 3.686 μg/m^3, and RMSPE increased by 4.125 and 3.131 μg/m^3, respectively for the GF model and MODIS DB model in Beijing. Analogously in Shanghai, R^2 decreased by 0.055 and 0.016, MPE increased by 5.246 and 0.267 μg/m^3, and RMSPE increased by 5.533 and 1.065 μg/m^3, respectively for the GF model and MODIS DB model. The results above indicated that the over-fitting level in MODIS DB model was relatively slighter than that in GF model, which was probably caused by an insufficient number of GF matched data per day (J. Hu et al., 2014; X. Hu et al., 2014). Overall, considering the R^2 for cross validation was relatively high in both the GF model and MODIS DB model, while the MPE and RMSPE were relatively low, this slight over-fitting could be neglected to some extent (Wu et al., 2016), and the $PM_{2.5}$ estimations by GF AOD and MODIS DB AOD were considered reliable. In addition to that, the DOY-based CV R^2 reached to 0.538, 0.578, and 0.500 for GF model in Wuhan, Beijing, and Shanghai, respectively, and the MPE and RMSPE were both relatively high. It should be mentioned that if there were less than two days that possessed enough matchups for modeling in one month, the datasets in this month would just be adopted for modeling. Thus, the number (N) of DOY-based CV was less than the original number for both MODIS DB model and GF model in Wuhan and Shanghai. In general, this was indeed not an ideal validation result. Nevertheless, the results could barely meet the requirement for application, which was much better than the lack of $PM_{2.5}$ estimation for the day. Through the nested model, additional 16 days of $PM_{2.5}$ estimations beyond the original 60 days in Wuhan, additional 15 days of $PM_{2.5}$ estimations beyond the original 76 days in Beijing, and additional 24 days of $PM_{2.5}$ estimations beyond the original 50 days in Shanghai were derived when there were not enough $PM_{2.5}$-AOD matchups for modeling on those days. Thus, it was practical to adopt the nested LME model to predict $PM_{2.5}$ in the days without $PM_{2.5}$-AOD matchups.

3.3. Estimation of $PM_{2.5}$ concentrations

The seasonal averaged $PM_{2.5}$ estimated using GF AOD in Wuhan, Beijing, and Shanghai are shown in Fig. 3, while the annual averaged $PM_{2.5}$ estimations and annual mean ground-level $PM_{2.5}$ measurements for each monitoring station are demonstrated in Fig. 4a–c and g–i, respectively. The annual averaged residuals at all monitoring stations in three cities were approximately 0. The annual averaged absolute residual at each monitoring station in Wuhan, Beijing, and Shanghai ranged from 10.326 to 10.981 μg/m^3, 11.282 to 12.537 μg/m^3, and 7.254 to 7.603 μg/m^3, respectively. In addition to that, the Moran's I for both seasonal and annual averaged absolute residuals in three cities were < 0.1 which indicated spatial autocorrelation hardly existed.

From the perspective of spatial distribution in annual averaged estimations, the ambient $PM_{2.5}$ concentrations were relatively high in the urban areas, which are mainly located in the center of Wuhan, the central and southern regions of Beijing, and the central and northwest regions of Shanghai. The ambient $PM_{2.5}$ concentrations were relatively low in the rural areas, mountainous areas, or coastal areas, especially in the northern and eastern regions of Wuhan, in northern and western regions of Beijing, and in southern and eastern regions of Shanghai. Directly from Fig. 4a, the red areas represented the urban comprehensive regions, while the blue-green areas corresponded to mountainous regions in Wuhan. In Fig. 4b, the red and orange areas showed the main urban comprehensive regions, while the blue-green areas represented mountainous areas in Beijing. From Fig. 4c, the red and orange areas represented part of the urban regions and industrial zones, while the blue-green areas corresponded to the rural areas and coastal areas in Shanghai.

In addition to that, the seasonal averaged estimations of $PM_{2.5}$ were studied using the same color bar, in order to highlight their seasonal variations. In Wuhan, severe $PM_{2.5}$ pollution occurred in winter, with over 120 μg/m^3 in whole regions because of the dense local emissions from heating combined with unfavorable meteorological diffusion conditions (Zhang et al., 2016d). Lower $PM_{2.5}$ concentrations occurred in summer, and the urban areas reached only 60 μg/m^3, which was caused by the more frequent precipitation and active atmospheric convection due to summer monsoon. In addition, intermediate situations appeared in spring and autumn when Wuhan tended to be affected by both local emissions and exogenous aerosols (Qian et al., 2008; Wu et al., 2011). Similar to the previous study in Beijing (Wu et al., 2016), high averaged $PM_{2.5}$ concentrations appeared in winter and spring, with over 110 and 90 μg/m^3 in most regions, respectively, with averaged $PM_{2.5}$ concentrations low in summer and average in autumn. Domestic heating in winter might be a primary cause of fine particle increasing (Zhao et al., 2015), while the dust storms from Northern and Eastern China in spring contributed to fine particle concentrations in Beijing (Han et al., 2015; Zheng et al., 2005). In Shanghai, the seasonal averaged $PM_{2.5}$ concentrations were relatively high in winter with most regions reaching up to 90 μg/m^3, relatively low in summer with most regions below 40 μg/m^3, and average in spring and autumn. The seasonal variation in Shanghai was mainly affected by the transport and dispersion of air mass, combined with dry and wet deposition (Wang et al., 2016; Ming et al., 2017). The prevailing wind during winter in Shanghai was from the north or northwest where the precursors were from the coal combustion for heating, which was the main reason for the higher $PM_{2.5}$ in winter of Shanghai. In comparison, the cleaner air mass from the East Sea of China and the higher mixing layer during summer in Shanghai provided favorable dilution conditions. Moreover, the seasonal variations of precipitation in Shanghai had influences on the wet deposition of $PM_{2.5}$ (Ding et al., 2013), and the dry deposition might also have impacts on the variations of $PM_{2.5}$ due to the seasonal patterns of deciduous plants (Zhang et al., 2001).

4. Discussion

4.1. Spatial resolution advantages of GF

The spatial resolution advantages of the GF $PM_{2.5}$ estimation were discussed by using current mainstream $PM_{2.5}$ estimations as references. The annual averaged $PM_{2.5}$ estimations during the experimental period using GF AOD in Wuhan, Beijing, and Shanghai are respectively illustrated in Fig. 4a, b, and c. And the annual averaged $PM_{2.5}$ estimations in these three cities based on MODIS DB AOD are respectively shown in Fig. 4e, f, and g. Although the GF $PM_{2.5}$ estimations and MODIS DB $PM_{2.5}$ estimations possessed approximately the same spatial distribution for the annual average, the GF estimations had an obvious advantage in the spatial resolution. For instance, the saltation in the $PM_{2.5}$ estimations of MODIS DB were distinct, whereas the GF $PM_{2.5}$ estimations illustrated a gradual variation in the spatial $PM_{2.5}$. In addition, the GF $PM_{2.5}$ estimations could distinguish the relatively small areas with the maximum $PM_{2.5}$ values, whereas MODIS DB could not detect these areas. These relatively small areas should have been explored because they can be considered $PM_{2.5}$ point emission sources. Therefore, GF AOD can provide more $PM_{2.5}$ variation details with much higher spatial resolution than MODIS DB AOD. Van et al., 2016 estimated the global ground-level $PM_{2.5}$ using satellite-based AOD with the GEOS-Chem chemical transport model, and the annual averaged satellite-derived $PM_{2.5}$ with $0.01^\circ \times 0.01^\circ$ spatial resolution was released on their website. The annual mean $PM_{2.5}$ estimations with 0.01° spatial

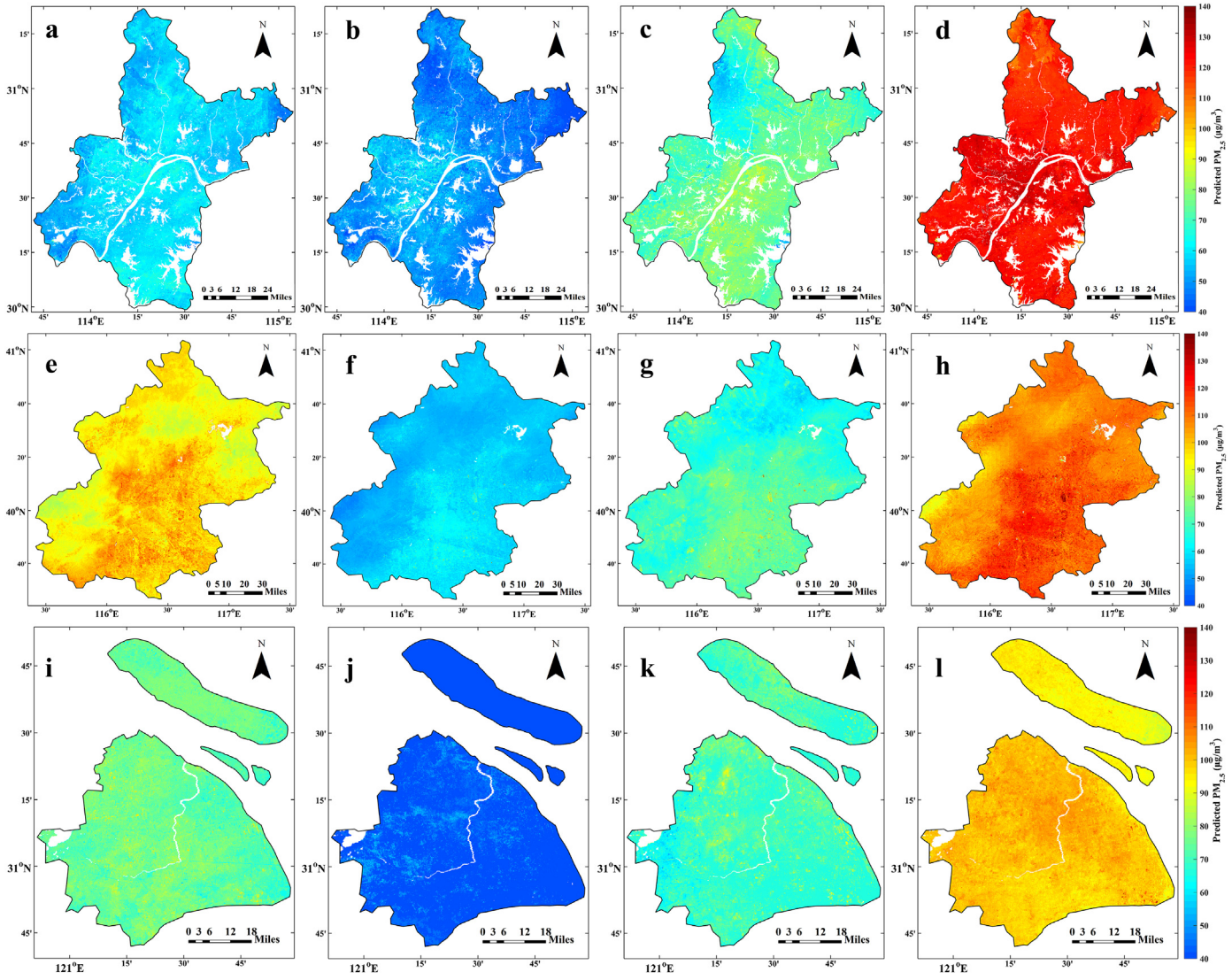

Fig. 3. Seasonally averaged $PM_{2.5}$ estimated by GF AOD in spring (a), summer (b), autumn (c), and winter (d) in Wuhan; seasonally averaged $PM_{2.5}$ estimated by GF AOD in spring (e), summer (f), autumn (g), and winter (h) in Beijing; seasonally averaged $PM_{2.5}$ estimated by GF AOD in spring (i), summer (j), autumn (k), and winter (l) in Shanghai.

resolution in Wuhan, Beijing, and Shanghai from 2014 to 2015 are illustrated in SI (Fig. S5, S6, and S7). Based on the details inside these high-resolution $PM_{2.5}$ estimations, it could merely show that $PM_{2.5}$ levels in part of urban areas in Wuhan and Beijing were high. However, western Wuhan, where rural areas are located, also possessed high levels of $PM_{2.5}$. And the $PM_{2.5}$ concentrations in Shanghai just declined along with the decrease in distance from the coastline, which hardly illustrated the urban inner $PM_{2.5}$ distribution in Shanghai. It was indicated that this $PM_{2.5}$ estimation with 0.01° spatial resolution had unsatisfactory performance in relative small regions, which could not be used to analyze the $PM_{2.5}$ pollution inside urban areas relating to urban structure.

4.2. Potential application in locating and quantifying main $PM_{2.5}$ emission sources of Wuhan

Compared to previous satellite $PM_{2.5}$ estimations, the GF $PM_{2.5}$ estimation has a unique spatial resolution advantage, which can offer new opportunities for exploring the $PM_{2.5}$ problem at a relatively small geographical scale. In general, field investigation and ground monitoring are adopted to locate $PM_{2.5}$ emission sources, then ground sampling and source apportionment analysis are adopted to quantify the contribution of different $PM_{2.5}$ emissions (Schauer et al., 1996; Zhang et al., 2013). To our knowledge, related urban $PM_{2.5}$ researches have not been carried out via remote sensing techniques because satellite-based atmospheric monitoring has relatively coarse spatial resolution, which leads to one pixel consisting of multiple urban landscapes. In this study, the extra value of ultrahigh resolution $PM_{2.5}$ was demonstrated through an application in locating main $PM_{2.5}$ emission sources and quantifying their contribution subsequently in Wuhan. And this application provides a new approach to study urban $PM_{2.5}$ emission sources, which can be easily applied in other urban regions.

Since the GF $PM_{2.5}$ estimation was $PM_{2.5}$ concentration instead of $PM_{2.5}$ emissions, the key point was that the spatial feature for $PM_{2.5}$ emissions should be highlighted, while the situation in which $PM_{2.5}$ concentrations fail to represent $PM_{2.5}$ emissions should be weakened. The process of automatically locating $PM_{2.5}$ emission sources was stated as follows. First, aiming at each pixel, the average process was conducted on daily value in these two years after excluding the maximum values and minimum values of 10% for this pixel. This step was to simply and partly solve two extreme cases, namely severe haze periods and excellent diffusion conditions, which resulted in high $PM_{2.5}$ pollution and low $PM_{2.5}$ concentration, respectively, at relative large scale. Therefore, the results of this adjusted annual averaged GF $PM_{2.5}$, which

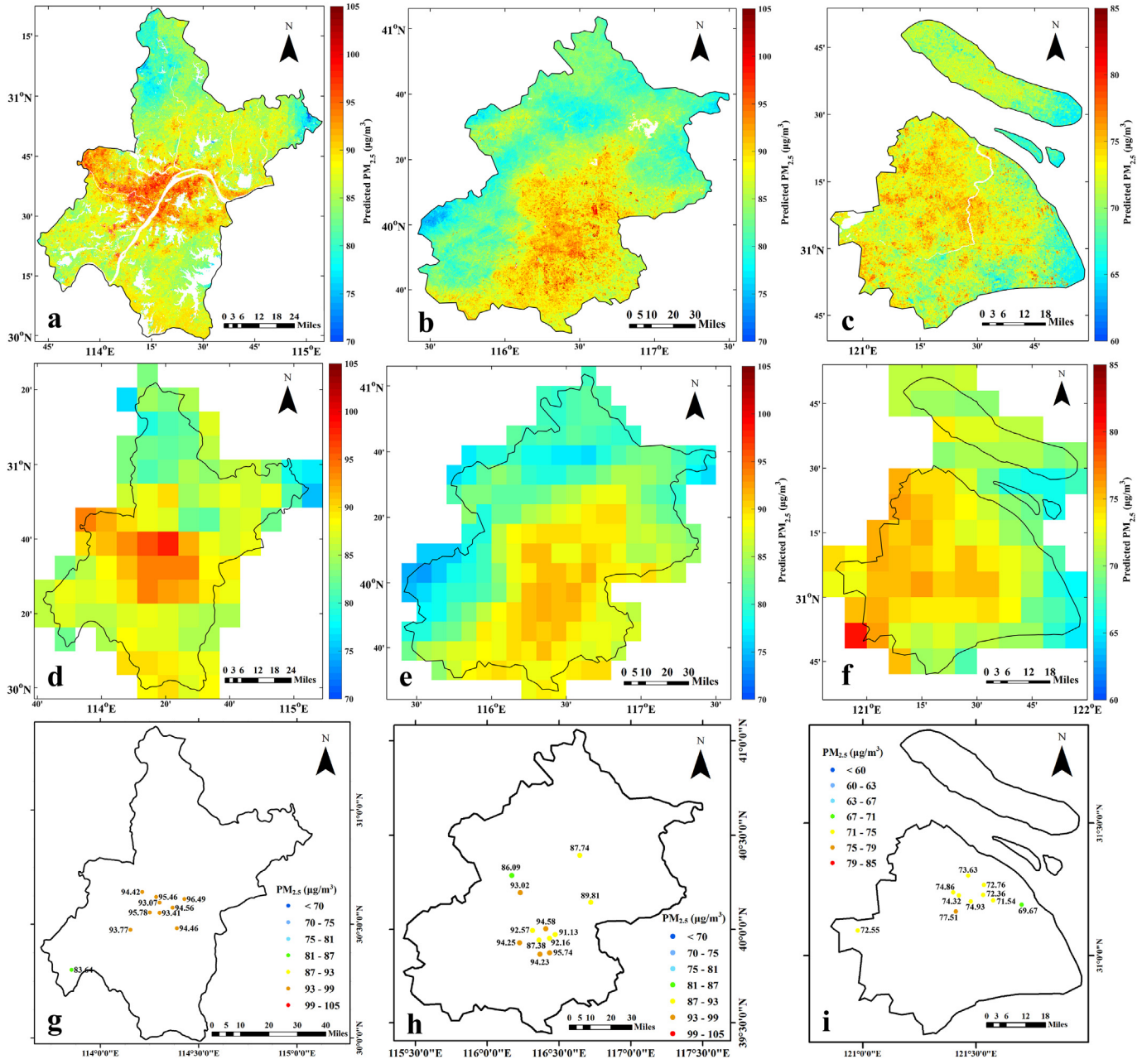

Fig. 4. Comparison of the $PM_{2.5}$ estimations using GF AOD (a, b, and c) and MODIS DB AOD (d, e, and f) in Wuhan (a, d, and g), Beijing (b, e, and h), and Shanghai (c, f, and i), respectively, combined with annual averaged ground-level $PM_{2.5}$ measurements at each monitoring station (g, h, and i). (For interpretation of the references to color in this figure, the reader is referred to the web version of this article.)

is shown in Fig. 5II, had more obvious spatial distinction than the original annual mean GF $PM_{2.5}$ estimation in Fig. 4a. Second, aiming at the whole region of Wuhan, the top 5% of the adjusted annual averaged GF $PM_{2.5}$ were selected to be the elemental pixels of the main $PM_{2.5}$ emission areas. In order to handle the noise pixels and the poor connectivity problem in the elemental pixels above, mathematical morphology methods, including open operation, close operation, and morphological reconstruction, were adopted based on binary elemental pixels. The results of automatically locating main $PM_{2.5}$ emission sources in Wuhan were illustrated via black lines in Fig. 5II, which were also shown in Google Earth image via red lines in Fig. 5I. Additionally, several typical details of locating areas were zoomed in upon in order to evaluate the performance of results. Fig. 5a outlined the center zone of urban areas where the confluence of the Yangtze and Han Rivers is located, and the cavities inside the urban center represented water covers or urban green spaces. Fig. 5b outlined the entire Tianhe International Airport, while only the parking apron and airstrip were selected as $PM_{2.5}$ emission area, indicating that our results could precisely distinguish $PM_{2.5}$ emission source inside a large $PM_{2.5}$ emissions unit to a certain extent. Fig. 5c outlined the combination of industrial zones and residential areas, in which the dividing line separated industrial zones from residential areas. Fig. 5d outlined a developing hi-tech industrial zone, which was previously a rural area before 2011. With approximately half of the buildings having been built from 2014 to 2015, our results accordingly reflected these $PM_{2.5}$ emission sources from urban construction. Apart from the situations above, a small number of industrial zones and residential areas were excluded by the process above due to their lower $PM_{2.5}$ emission loads and less population density, respectively. In summary, the automatically demarcated areas in this study could precisely locate main $PM_{2.5}$ emission sources,

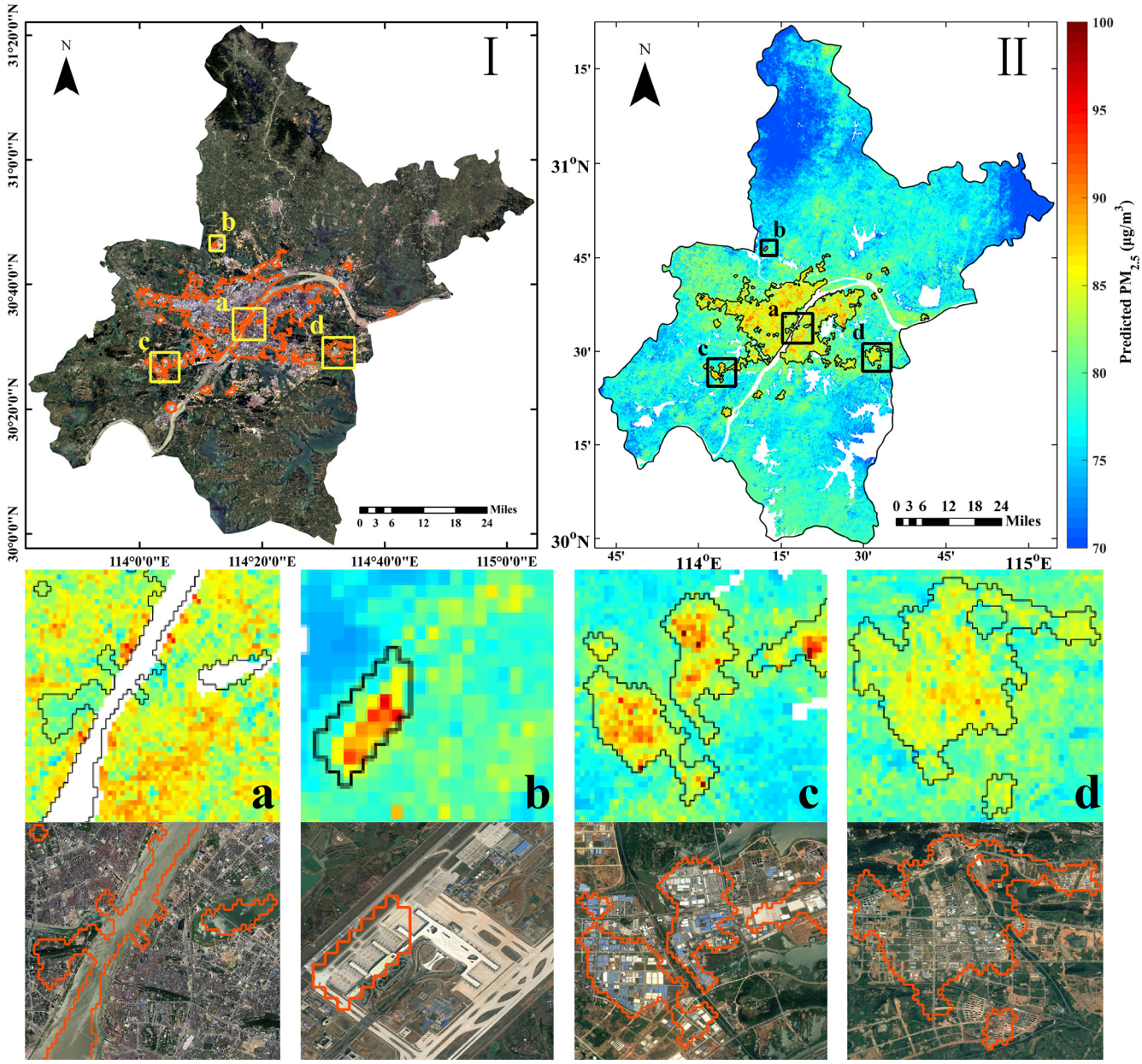

Fig. 5. Results and performances of automatically locating main $PM_{2.5}$ emission sources in Wuhan via the adjusted annual averaged GF $PM_{2.5}$ estimation, combined with Google Earth images as references.

consisting of urban centers, transportation hubs, industrial zones, and urban construction.

In total, 28 elemental urban sections were identified based on automatically demarcated $PM_{2.5}$ emission source areas in Wuhan (Fig. 6), depending on both field investigation and Google Earth image sequences. The details of field investigation are shown in Table 3. The comprehensive zones, where dense residential areas, business zones, and urban construction were predominant, consist of Hankou Town (No. 1), Hanyang Town (No. 2), and Wuchang Town (No. 3). The Hankoubei Business and Trade Center (No. 4) was the biggest business zone outside the outer ring road and was recognized as a vital $PM_{2.5}$ emissions source. According to the comparison of temporal sequence satellite images from 2014 to 2015, the green regions in Fig. 6 were considered as $PM_{2.5}$ emission sources from urban construction. In addition, as a typical industrial city in central China, most of the industrial zones had been relocated to outside the outer ring road of Wuhan, which in turn caused industrial $PM_{2.5}$ pollution surrounding the urban comprehensive zones.

From the perspective of industrial structure, the secondary industry was allocated in large proportion, such as electricity, iron and steel, building materials, automobile manufacturing, and chemicals. However, the high-tech industries were still under development merely in the Guanggu economic and technological development zone (No. 16) in recent years. This unreasonable industrial structure directly resulted in a distinct industrial contribution to $PM_{2.5}$ emissions in Wuhan. To quantify the contribution proportion of local $PM_{2.5}$ emission sources, it is of vital significance to adopt an index to measure their contribution. Previous studies generally adopted source apportionment methodology to analyze the chemical compositions and emission sources of $PM_{2.5}$ (Querol et al., 2001; Zheng et al., 2002; Zheng et al., 2005). Nevertheless, no matter what kind of source apportionment cannot skip massive sampling, which possesses a high cost of human resources and financial resources. It should also be noted that site-based sampling could not represent the overall situation in the whole region. Based on

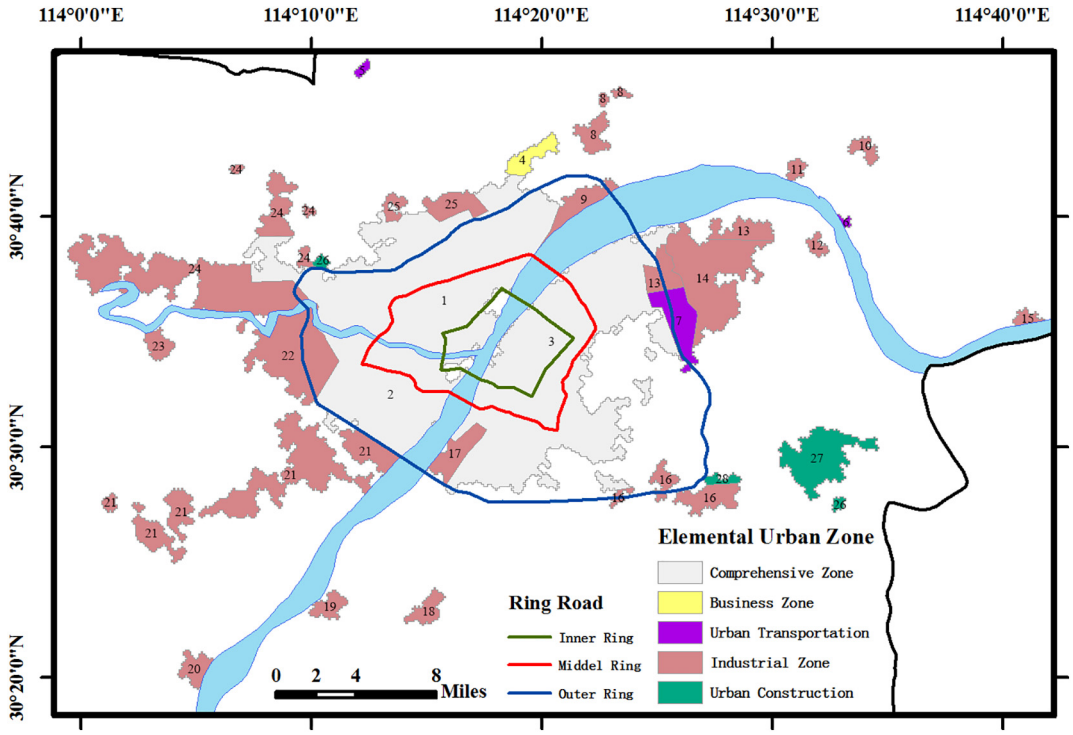

Fig. 6. Field investigation of demarcated $PM_{2.5}$ emission sources with primary urban function in Wuhan.

our results above, the contribution to $PM_{2.5}$ emissions can be quantified via remote sensing techniques. Accordingly, the Total $PM_{2.5}$ Emission Index (TPMEI), which was simply the sum of the adjusted averaged $PM_{2.5}$ in one demarcated region, was proposed and calculated to represent the $PM_{2.5}$ emission level from that demarcated area in Table 2. Taking industrial zones as an example, the proportion of industrial contribution to $PM_{2.5}$ emissions in Wuhan was the sum of the TPMEI in industrial zones divided by the sum of the TPMEI in all elemental zones, namely 37.77%. Based on positive matrix factor (PMF) analysis (Cheng et al., 2012), the source apportionment results of local $PM_{2.5}$ from the end of 2013 to early 2016 were released by the Wuhan Environmental Protection Bureau in April 2016 (WEPB, 2016). The results showed that the emissions from industrial production accounted for 32% of $PM_{2.5}$ local emissions, proving that evaluating the $PM_{2.5}$ contribution proportion of different elemental zone from TPMEI was acceptable. Meanwhile, it was found that approximately 56.16% of local $PM_{2.5}$

Table 3
List of elemental urban zones in $PM_{2.5}$ emission areas of Wuhan, combined with the Total $PM_{2.5}$ Emission Index (TPMEI) as a $PM_{2.5}$ emissions contribution factor.

No.	Location	Area (km^2)	TPMEI ($1 \times 10^3 \mu g\, m^{-3} km^2$)
1	Hankou Town	174.259	14.863
2	Hanyang Town	74.317	6.290
3	Wuchang Town	178.944	15.084
4	Hankoubei Business and Trade Center	6.118	0.522
5	Wuhan Tianhe International Airport	1.024	0.087
6	Wuhan Yangluo Wharf	1.254	0.105
7	Wuhan High-speed Railway Station & Bullet Train Maintenance Base	12.979	1.125
8	Hankoubei Industrial Base of Building and Decoration Materials	6.963	0.588
9	Wuhan Chenjiaji Industrial Zone	11.469	0.973
10	Wuhan Yangluo Industrial Zone	2.842	0.235
11	Wuhan Iron and Steel Group Company Limited, Jiangbei Branch	1.997	0.168
12	Sinopec Wuhan Petrochemical Company Limited	1.997	0.169
13	Wuhan Qingshan Industrial Zone	6.989	0.604
14	Wuhan Iron and Steel Group Company Limited	37.146	3.120
15	Shuangliu Production Base of Heavy Industry	7.962	0.670
16	Wuhan Guanggu Economic and Technological Development Zone	12.877	1.079
17	Wuhan Baishazhou Economic Development Zone	9.318	0.792
18	Wuhan Jiangxia Industrial Zone	4.531	0.377
19	Wuhan Jiangxia Automobile Production and Distribution Center	4.045	0.346
20	Wuhan Huading Industrial Zone	6.246	0.527
21	Wuhan Zhuankou Economic and Technological Development Zone	56.909	4.807
22	Wuhan Huangjinkou Industrial Zone	34.330	2.929
23	Wuhan Jiahe Industrial Zone	3.866	0.326
24	Wuhan Dongxihu Economic Development Zone	68.685	5.816
25	Wuhan Jinyintan Industrial Zone	9.907	0.845
26	Peripherally Dilated Residential Area	1.894	0.157
27	Developing Hi-Tech Industrial Zone	21.094	1.760
28	Guanggu International Olympic Sports Center	1.946	0.161

emissions in Wuhan stemmed from comprehensive zones, which were the result of intensive human activity and dense urban construction. Based on this index, the analysis of $PM_{2.5}$ emission contributions was thereby related to the urban landscape and functional zones instead of chemical component analysis. In other words, the fine particle pollution in inner urban areas could also be explored and analyzed via remote sensing techniques. This index was easily calculated and could be widely used to assess $PM_{2.5}$ emission contributions in other urban regions without $PM_{2.5}$ source apportionment. Along with joint observations via other high-resolution satellites, such as Gaofen-2 and Gaofen-4, the temporal resolution of GF $PM_{2.5}$ could further increase, and the $PM_{2.5}$ emission contribution could be calculated every year to evaluate the efficacy of emission reduction policies in urban area.

Furthermore, this study attempted to connect the daily GF $PM_{2.5}$ estimation with ground-monitor pollutant gas emissions in non-haze period, and the GF $PM_{2.5}$ thereby became a complementary method to monitor pollutant gas emission loads in some specific situations. This specific condition in the experiment was also set to rule out windy period, which excluded good diffusion condition that facilitated pollutant dispersion. Table 4 demonstrated the Pearson correlation coefficient between daily GF $PM_{2.5}$ estimation and pollutant gas emissions from 7 key emission sources in Wuhan, combined with the information and location of these key emission sources. The daily pollutant gas emissions, including SO_2 and NO_x, were monitored and released by the Hubei Provincial Environmental Protection Bureau (Environmental Information Release System of Pollution Source in Hubei Province: http://119.97.194.18:4508/). The Pearson correlation coefficient, which is a measure of the linear correlation between two variables, has been adopted to calculate the correlation between GF $PM_{2.5}$ and SO_2/NO_x. Its value ranges from -1 to $+1$, where -1 means an absolutely negative correlation, 0 means no correlation, and $+1$ means an absolutely positive correlation. According to the results in Table 4, GF $PM_{2.5}$ had positive correlation with pollutant gas emissions at all emission sources. The ideal Pearson correlation coefficient reached up to 0.6, even 0.7, while the coefficient of State Power Qingshan Thermal Power Co. Ltd. and Wuhan Iron and Steel Group Co. Ltd. showed weak positive correlations. The possible reason was they were all located in Wuhan iron and steel industrial zones, which contained multiple exhaust stacks of pollutant gas. When these exhaust stacks were close to each other, the results would be influenced by cross effects. In general, the daily GF $PM_{2.5}$ estimation possessed positive correlation with pollutant gas emission loads, which could offer an auxiliary approach to quantify daily $PM_{2.5}$ emission levels without ground monitoring stations in non-haze period.

In sum, GF $PM_{2.5}$ estimation with ultrahigh spatial resolution provides a unique perspective for locating and quantifying urban $PM_{2.5}$ emission sources through remote sensing techniques. The spatial construction of urban inner fine particle pollution could be related to urban unit at a relative small scale, and the $PM_{2.5}$ emissions could also be linked to the urban function areas. The experimental results indicate that GF $PM_{2.5}$ can support to precisely locate main $PM_{2.5}$ emission sources, evaluate local $PM_{2.5}$ contribution proportion, and quantify daily $PM_{2.5}$ emission levels in non-haze period to a certain extent. Corresponding studies in previous literature could only be conducted through massive ground sampling, chemical component analysis, and $PM_{2.5}$ source apportionment, which consumed plenty of manpower and financial resources. Thus, analyzing urban inner $PM_{2.5}$ via GF can be considered as a convenient and efficient approach, and it is feasible to apply it widely in other cities.

4.3. Limitations and future work

In this study, we used the GF AOD retrievals to estimate the ground-level $PM_{2.5}$ mass concentrations in three representative cities of China, combined with the WRF meteorologically simulated data. To our knowledge, this is one of the first study that estimates $PM_{2.5}$ concentrations in urban areas with an ultrahigh spatial resolution of 160 m. Compared to the estimates from conventional moderate resolution satellites, GF $PM_{2.5}$ estimations have very high spatial resolution. Therefore, these data could be used to locate $PM_{2.5}$ emission sources, and many additional applications related to urban landscape and $PM_{2.5}$ pollution structures could be developed based on the ultrahigh resolution $PM_{2.5}$ estimations.

There exist limitations should be discussed. The first limitation is the limited number of AOD-$PM_{2.5}$ matchups per day. It was proven that fewer matchups would cause model over-fitting and deteriorate the estimation accuracy, and over-fitting was alleviated with an increasing number of matchups per day (J. Hu et al., 2014; X. Hu et al., 2014; Wu et al., 2016). According to the lack of AOD retrievals mainly caused by cloud obscuration, in this paper, a minimum daily number of three matchups was required to ensure both sufficient number of observations in the CV model and prediction accuracy. Meanwhile, the uniform spatial distribution for $PM_{2.5}$ monitoring stations is necessary to more accurately predict the $PM_{2.5}$ level over rural and mountainous areas, because most of the monitoring sites are located in urban regions. Second, since the experimental regions in this study were relatively small, little spatial variation occurred in the relationship between $PM_{2.5}$ and AOD. Our results demonstrated little spatial autocorrelation in the residuals of the $PM_{2.5}$ estimations. However, with the expansion of the $PM_{2.5}$ estimation region, spatial variation will become prominent and should no longer be neglected. Therefore, we plan to use a second-stage geo-statistics model by adopting the residuals of the first-stage LME model as a dependent variable and using the geographic-related parameters as independent variables in order to estimate the $PM_{2.5}$ concentrations with ultrahigh spatial resolution at a larger scale. Thirdly, it should be noted that the $PM_{2.5}$ estimations in those days without enough AOD-$PM_{2.5}$ matchups possessed the same weight as the original $PM_{2.5}$ estimations when calculating seasonal and annual $PM_{2.5}$ estimations in this study. However, since $PM_{2.5}$ estimates in those days with or without $PM_{2.5}$-AOD matchups have different accuracy, it would be better to assign different weights to different daily $PM_{2.5}$ estimations. Fourthly, it also should be mentioned that the GF AOD was good enough to locate atmospheric pollution sources, which was demonstrated in our previous study (Sun et al., 2018). However, the atmospheric pollution sources located by GF AOD included both fine particle and coarse particle emission sources, which could not be adopted to apply

Table 4
The Pearson correlation coefficient between the daily GF $PM_{2.5}$ estimation and pollutant gas emissions from 7 key emission source monitoring sites in Wuhan.

Site	Longitude	Latitude	N	Pearson coef. ($PM_{2.5}$-SO_2)	Pearson coef. ($PM_{2.5}$-NO_X)
Wuhan Gaoxin Thermo Power Co. Ltd.	114.4210	30.4832	23	0.705	0.679
Wuhan Chenming Qianneng Thermo Power Co. Ltd.	114.1937	30.4785	17	0.654	0.601
Wuhan Branch of China Petrochemical Co. Ltd.	114.4307	30.6517	18	0.506	0.612
State Power Qingshan Thermal Power Co. Ltd. (*Furnace 12#*)	114.4358	30.6345	19	0.312	0.418
State Power Qingshan Thermal Power Co. Ltd. (*Furnace 13#*)	114.4378	30.6328	21	0.533	0.341
Wuhan Iron and Steel Group Co. Ltd. (*Four Sintering Desulfurization Furnace*)	114.4350	30.6318	19	0.355	0.469
Wuhan Iron and Steel Electricity Co. Ltd.	114.4649	30.6394	19	0.76	0.783

in locating and quantifying $PM_{2.5}$ emission sources. Finally, due to its high resolution, the GF-1 WFV has a revisit period of four days, which indicates an apparent limitation in the temporal resolution. To better capture the $PM_{2.5}$ temporal variation trends, our future work will focus on constructing a high-resolution satellite air monitoring network in China, which preliminarily consists of Gaofen-1, Gaofen-2 (a sun synchronous recurrent satellite launched in 2014 with the same multi-spectral bands as GF-1), and Gaofen-4 (a geosynchronous satellite launched in 2015 with the same multi-spectral bands as GF-1) and may be extended to incorporate Landsat-8 (launched in 2013 with no existing AOD retrieval algorithm).

5. Conclusions

This paper first evaluates the feasibility of estimating ground-level $PM_{2.5}$ in urban areas using the 160 m spatial resolution GF AOD and nested LME model. The results show that the performance of the GF-estimated $PM_{2.5}$ concentrations at a 160 m spatial resolution is comparable to that of the MODIS DB-estimated $PM_{2.5}$ at a 10 km spatial resolution. It was demonstrated that the ultrahigh spatial resolution of GF AOD products offers substantial advantages over current mainstream $PM_{2.5}$ estimations by providing spatially finer contrasts of $PM_{2.5}$ trends and relating to smaller geographical units. Based on this ultrahigh spatial resolution, GF $PM_{2.5}$ estimations provide a unique perspective for locating and quantifying urban $PM_{2.5}$ emission sources through remote sensing techniques. The experimental results indicate that GF $PM_{2.5}$ can help to precisely locate main $PM_{2.5}$ emission sources, evaluate local $PM_{2.5}$ contribution proportion, and quantify daily $PM_{2.5}$ emission levels in non-haze period to a certain extent. Along with joint observations using other high-resolution satellites, GF $PM_{2.5}$ will gradually become a convenient approach to analyze the urban inner $PM_{2.5}$ problem and offer an efficient way for government to evaluate the efficacy of emission management and reduction policies in urban areas.

Our future studies will focus on three aspects. First, we will try to estimate ultrahigh resolution $PM_{2.5}$ concentrations at larger scale by developing a second-stage geo-statistics model based on the residuals of the LME model and considering spatial variation. Second, we will relate the ultrahigh resolution $PM_{2.5}$ estimations to multiple types of urban structures and landscapes to analyze the urban inner pollution patterns and wind corridors. Finally, since the $PM_{2.5}$ estimations using GF-1 AOD have limited temporal resolution, we plan to apply our GF AOD retrieval algorithm to Gaofen-2 and Gaofen-4, which have the same multi-spectral bands as GF-1 and constitute high-resolution satellite air monitoring network in China.

Acknowledgements

This study was supported financially by the National Key R&D Program of China (Nos. 2017YFC0212601, 2016YFC0200900), the Hubei Provincial Natural Science Foundation of China (No. 2016CFB620), the National Natural Science Foundation of China (No. 41571344), and the China Postdoctoral Science Foundation (No. 2015M572198). We express our sincere gratitude to the anonymous reviewers and the editor for their constructive comments.

Appendix A. Supplementary data

Supplementary data to this article can be found online at https://doi.org/10.1016/j.rse.2018.06.030.

References

Bai, Y., Wu, L., Qin, K., Zhang, Y., Shen, Y., Zhou, Y., 2016. A geographically and temporally weighted regression model for ground-level $PM_{2.5}$ estimation from Satellite-derived 500 m resolution AOD. Remote Sens. 8, 262.

Beelen, R., Raaschou-Nielsen, O., Stafoggia, M., Andersen, Z.J., Weinmayr, G., Hoffmann, B., Wolf, K., Samoli, E., Fischer, P., Nieuwenhuijsen, M., 2014. Effects of long-term exposure to air pollution on natural-cause mortality: an analysis of 22 European cohorts within the multicentre ESCAPE project. Lancet 383, 785–795.

Chang, H.H., Hu, X., Liu, Y., 2013. Calibrating MODIS aerosol optical depth for predicting daily $PM_{2.5}$ concentrations via statistical downscaling. J. Expo. Sci. Environ. Epidemiol. 1–7.

Che, H., Xia, X., Zhu, J., Li, Z., Dubovik, O., Holben, B., Goloub, P., Chen, H., Estelles, V., Cuevasagulló, E., 2014. Column aerosol optical properties and aerosol radiative forcing during a serious haze-fog month over North China Plain in 2013 based on ground-based sunphotometer measurements. Atmos. Chem. Phys. 14, 2125–2138.

Cheng, H., Wang, Z., Feng, J., Chen, H., Zhang, F., Liu, J., 2012. Carbonaceous species composition and source apportionment of $PM_{2.5}$ in urban atmosphere of Wuhan. Ecol. Environ. Sci. 21, 1574–1579.

China, M. E. P, 2012. Ambient Air Quality Standards. GB 3095–2012. China Environmental Science Press, Beijing.

Chu, D.A., Kaufman, Y.J., Zibordi, G., Chern, J.D., Mao, J., Li, C., Holben, B.N., 2003. Global monitoring of air pollution over land from the Earth Observing System-Terra Moderate Resolution Imaging Spectroradiometer (MODIS). J. Geophys. Res. 108, 4661.

Chudnovsky, A., Tang, C., Lyapustin, A., Wang, Y., Schwartz, J., Koutrakis, P., 2013. A critical assessment of high resolution aerosol optical depth (AOD) retrievals for fine particulate matter (PM) predictions. Atmos. Chem. Phys. 13, 10907–10917.

Chudnovsky, A.A., Koutrakis, P., Kloog, I., Melly, S., Nordio, F., Lyapustin, A., Wang, Y., Schwartz, J., 2014. Fine particulate matter predictions using high resolution Aerosol Optical Depth (AOD) retrievals. Atmos. Environ. 89, 189–198.

Dawson, J.P., Adams, P.J., Pandis, S.N., 2007. Sensitivity of $PM_{2.5}$ to climate in the Eastern US: a modeling case study. Atmos. Chem. Phys. 7, 4295–4309.

Ding, A., Fu, C., Yang, X., Sun, J., Zheng, L., Xie, Y., Herrmann, E., Petaja, T., Kerminen, V.M., Kulmala, M., 2013. Ozone and fine particle in the western Yangtze River Delta: an overview of 1 yr data at the SORPES station. Atmos. Chem. Phys. 13, 5813–5830.

Dockery, D.W., Xu, X., Spengler, J.D., Ware, J.H., Fay, M.E., Ferris Jr., B., Speizer, F.E., 1993. An association between air pollution and mortality in six U.S. cities. N. Engl. J. Med. 329, 1753–1759.

Engelcox, J.A., Hoff, R.M., Haymet, A.D., 2004. Recommendations on the use of satellite remote-sensing data for urban air quality. J. Air Waste Manage. Assoc. 54, 1360–1371.

Feng, L., Li, J., Gong, W., Zhao, X., Chen, X., Pang, X., 2016. Radiometric cross-calibration of Gaofen-1 WFV cameras using Landsat-8 OLI images: a solution for large view angle associated problems. Remote Sens. Environ. 174, 56–68.

Ghotbi, S., Sotoudeheian, S., Arhami, M., 2016. Estimating urban ground-level PM_{10} using MODIS 3km AOD product and meteorological parameters from WRF model. Atmos. Environ. 141, 333–346.

Gupta, P., Christopher, S.A., Wang, J., Gehrig, R., Lee, Y., Kumar, N., 2006. Satellite remote sensing of particulate matter and air quality assessment over global cities. Atmos. Environ. 40, 5880–5892.

Han, L., Zhou, W., Li, W., Li, L., 2014. Impact of urbanization level on urban air quality: a case of fine particles ($PM_{2.5}$) in Chinese cities. Environ. Pollut. 194, 163–170.

Han, L., Cheng, S., Zhuang, G., Ning, H., Wang, H., Wei, W., Zhao, X., 2015. The changes and long-range transport of $PM_{2.5}$ in Beijing in the past decade. Atmos. Environ. 110, 186–195.

Hoek, G., Krishnan, R.M., Beelen, R., Peters, A., Ostro, B., Brunekreef, B., Kaufman, J.D., 2013. Long-term air pollution exposure and cardio- respiratory mortality: a review. Environ. Health 12 (43). http://dx.doi.org/10.1186/1476-069X-12-43.

Hu, X., Waller, L.A., Al-Hamdan, M.Z., Crosson, W.L., Estes Jr., M.G., Estes, S.M., Quattrochi, D.A., Sarnat, J.A., Liu, Y., 2013a. Estimating ground-level $PM_{2.5}$ concentrations in the southeastern U.S. using geographically weighted regression. Environ. Res. 121, 1–10.

Hu, X., Waller, L.A., Lyapustin, A., Wang, Y., Liu, Y., 2013b. 10 yr spatial and temporal trends of $PM_{2.5}$ concentrations in the southeastern US estimated using high-resolution satellite data. Atmos. Chem. Phys. 13, 25617–25648.

Hu, J., Wang, Y., Ying, Q., Zhang, H., 2014. Spatial and temporal variability of $PM_{2.5}$ and PM_{10} over the North China Plain and the Yangtze River Delta, China. Atmos. Environ. 95, 598–609.

Hu, X., Waller, L.A., Lyapustin, A., Wang, Y., Al-Hamdan, M.Z., Crosson, W.L., Estes Jr., M.G., Estes, S.M., Quattrochi, D.A., Puttaswamy, S.J., 2014. Estimating ground-level $PM_{2.5}$ concentrations in the southeastern United States using MAIAC AOD retrievals and a two-stage model. Remote Sens. Environ. 140, 220–232.

Huete, A., Didan, K., Miura, T., Rodriguez, E.P., Gao, X., Ferreira, L.G., 2002. Overview of the radiometric and biophysical performance of the MODIS vegetation indices. Remote Sens. Environ. 83 (1), 195–213.

Just, A.C., Wright, R.O., Schwartz, J., Coull, B.A., Baccarelli, A.A., Tellez-Rojo, M.M., Moody, E., Wang, Y., Lyapustin, A., Kloog, I., 2015. Using high-resolution satellite aerosol optical depth to estimate daily $PM_{2.5}$ geographical distribution in Mexico City. Environ. Sci. Technol. 49, 8576.

Kohavi, R., 2001. A study of cross-validation and bootstrap for accuracy estimation and model selection. In: Proceedings from International Joint Conference on Artificial Intelligence. 14(2). pp. 1137–1143.

Lee, H.J., Liu, Y., Coull, B.A., Schwartz, J., Koutrakis, P., 2011. A novel calibration approach of MODIS AOD data to predict $PM_{2.5}$ concentrations. Atmos. Chem. Phys. 11 (11), 9769–9795.

Levy, R.C., Mattoo, S., Munchak, L.A., Remer, L.A., 2013. The collection 6 MODIS aerosol products over land and ocean. Atmos. Meas. Tech. 6, 2989–3034.

Li, Z., Feng, N., Kwon-Ho, L., Xin, J., Hao, W.M., Bryce, N., Wang, Y., Wang, P., 2007.

Validation and understanding of moderate resolution imaging spectroradiometer aerosol products (C5) using ground-based measurements from the handheld Sun photometer network in China. J. Geophys. Res. 112, 365–371.
Li, C., Hsu, N.C., Tsay, S.C., 2011. A study on the potential applications of satellite data in air quality monitoring and forecasting. Atmos. Environ. 45, 3663–3675.
Li, Z., Shen, H., Li, H., Xia, G., Gamba, P., Zhang, L., 2017. Multi-feature combined cloud and cloud shadow detection in GaoFen-1 wide field of view imagery. Remote Sens. Environ. 191, 342–358.
Lin, C., Li, Y., Yuan, Z., Lau, A.K., Li, C., Fung, J.C., 2015. Using satellite remote sensing data to estimate the high-resolution distribution of ground-level $PM_{2.5}$. Remote Sens. Environ. 156, 117–128.
Liu, Y., Sarnat, J.A., Kilaru, V., Jacob, D.J., Koutrakis, P., 2005. Estimating ground-level $PM_{2.5}$ in the eastern United States using satellite remote sensing. Environ. Sci. Technol. 39, 3269–3278.
Liu, Y., Franklin, M., Kahn, R., Koutrakis, P., 2007a. Using aerosol optical thickness to predict ground-level $PM_{2.5}$ concentrations in the St. Louis area: a comparison between MISR and MODIS. Remote Sens. Environ. 107, 33–44.
Liu, Y., Koutrakis, P., Kahn, R., 2007b. Estimating fine particulate matter component concentrations and size distributions using satellite-retrieved fractional aerosol optical depth: part 1—method development. J. Air Waste Manage. Assoc. 57, 1351–1359.
Liu, Y., Koutrakis, P., Kahn, R., Turquety, S., Yantosca, R.M., 2007c. Estimating $PM_{2.5}$ component concentrations and size distributions using satellite-retrieved fractional aerosol optical depth: part 2—a case study. J. Air Waste Manage. Assoc. 57, 1360–1369.
Luo, N., Man, S.W., Zhao, W., Yan, X., Xiao, F., 2015. Improved aerosol retrieval algorithm using Landsat images and its application for PM_{10} monitoring over urban areas. Atmos. Res. 153, 264–275.
Lyapustin, A., Martonchik, J., Wang, Y., Laszlo, I., Korkin, S., 2011a. Multiangle implementation of atmospheric correction (MAIAC): 1. Radiative transfer basis and look-up tables. J. Geophys. Res. Atmos. 116, D03210.
Lyapustin, A., Wang, Y., Laszlo, I., Kahn, R., Korkin, S., Remer, L., Levy, R., Reid, J.S., 2011b. Multi-angle implementation of atmospheric correction (MAIAC): 2. Aerosol algorithm. J. Geophys. Res. Atmos. 116, 613–632.
Lyapustin, A.I., Wang, Y., Laszlo, I., Hilker, T., Hall, F.G., Sellers, P.J., Tucker, C.J., Korkin, S.V., 2012. Multi-angle implementation of atmospheric correction for MODIS (MAIAC): 3. Atmospheric correction. Remote Sens. Environ. 127, 385–393.
Ma, Z., Liu, Y., Zhao, Q., Liu, M., Zhou, Y., Bi, J., 2016. Satellite-derived high resolution $PM_{2.5}$ concentrations in Yangtze River Delta Region of China using improved linear mixed effects model. Atmos. Environ. 133, 156–164.
Man, S.W., Nichol, J.E., Lee, K.H., 2011. An operational MODIS aerosol retrieval algorithm at high spatial resolution, and its application over a complex urban region. Atmos. Res. 99, 579–589.
Ming, L., Jin, L., Li, J., Fu, P., Yang, W., Liu, D., Zhang, G., Wang, Z., Li, X., 2017. $PM_{2.5}$ in the Yangtze River Delta, China: chemical compositions, seasonal variations, and regional pollution events. Environ. Pollut. 223, 200–212.
Nowak, D.J., Crane, D.E., Stevens, J.C., 2006. Air pollution removal by urban trees and shrubs in the United States. Urban For. Urban Green. 4 (3), 115–123.
Oo, M.M., Ross, A., Holz, R., Holloway, T., Ackerman, S.A., 2013. Investigating Cloud Contamination in MODIS and VIIRS AOD Retrievals and the Impacts on Air Quality Applications. In: Proceedings from AGU Fall Meeting.
Pinto, J.P., Lefohn, A.S., Shadwick, D.S., 2004. Spatial variability of $PM_{2.5}$ in urban areas in the United States. J. Air Waste Manage. Assoc. 54, 440–449.
Pope 3rd, C.A., Burnett, R.T., Thun, M.J., Calle, E.E., Krewski, D., Ito, K., Thurston, G.D., 2002. Lung cancer, cardiopulmonary mortality, and long-term exposure to fine particulate air pollution. JAMA 287, 1132–1141.
Pugh, T.A.M., MacKenzie, A.R., Whyatt, J.D., Hewitt, C.N., 2012. Effectiveness of green infrastructure for improvement of air quality in urban street canyons. Environ. Sci. Technol. 46, 7692–7699.
Qian, Z., He, Q., Lin, H.M., Kong, L., Bentley, C.M., Liu, W., Zhou, D., 2008. High temperatures enhanced acute mortality effects of ambient particle pollution in the "oven" city of Wuhan, China. Environ. Health Perspect. 116, 1172–1178. http://dx.doi.org/10.1289/ehp.10847.
Qian, D., Kloog, I., Koutrakis, P., Lyapustin, A., Wang, Y., Schwartz, J., 2016. Assessing $PM_{2.5}$ exposures with high spatio-temporal resolution across the continental United States. Environ. Sci. Technol. 50.
Qiao, T., Zhao, M., Xiu, G., Yu, J., 2016. Simultaneous monitoring and compositions analysis of PM_1 and $PM_{2.5}$ in Shanghai: implications for characterization of haze pollution and source apportionment. Sci. Total Environ. 557–558, 386–394.
Querol, X., Alastuey, A., Rodriguez, S., Plana, F., Ruiz, C.R., Cots, N., Puig, O., 2001. PM_{10} and $PM_{2.5}$ source apportionment in the Barcelona Metropolitan area, Catalonia, Spain. Atmos. Environ. 35 (36), 6407–6419.
Sacks, J.D., Stanek, L.W., Luben, T.J., Johns, D.O., Buckley, B.J., Brown, J.S., Ross, M., 2011. Particulate matter-induced health effects: who is susceptible? Environ. Health Perspect. 119, 446–454.
Schauer, J.J., Rogge, W.F., Hildemann, L.M., Mazurek, M.A., Cass, G.R., Simoneit, B.R., 1996. Source apportionment of airborne particulate matter using organic compounds as tracers. Atmos. Environ. 30 (22), 3837–3855.
Song, W., Jia, H., Huang, J., Zhang, Y., 2014. A satellite-based geographically weighted regression model for regional $PM_{2.5}$ estimation over the Pearl River Delta region in China. Remote Sens. Environ. 154, 1–7.
Song, J., Guang, W., Li, L., Xiang, R., 2016. Assessment of air quality status in Wuhan, China. Atmosphere 7, 56.
Sun, K., Chen, X., Zhu, Z., Zhang, T., 2017. High resolution aerosol optical depth retrieval using gaofen-1 WFV camera data. Remote Sens. 9, 89.
Sun, K., Chen, X., Wang, J., Zhang, T., Zhu, Z., 2018. Investigation of air quality over the largest city in Central China using high resolution satellite derived aerosol optical depth data. Atmos. Pollut. Res. 9 (3), 584–593.
Tai, A., Mickley, L., Jacob, D., 2010. Correlations between fine particulate matter ($PM_{2.5}$) and meteorological variables in the United States: implications for the sensitivity of $PM_{2.5}$ to climate change. Atmos. Environ. 44 (32), 3976–3984.
Van, D.A., Martin, R.V., Spurr, R.J., Burnett, R.T., 2015. High-resolution satellite-derived $PM_{2.5}$ from optimal estimation and geographically weighted regression over North America. Environ. Sci. Technol. 49, 10482–10491.
Van, D.A., Martin, R.V., Brauer, M., Hsu, N.C., Kahn, R.A., Levy, R.C., Winker, D.M., 2016. Global estimates of fine particulate matter using a combined geophysical-statistical method with information from satellites, models, and monitors. Environ. Sci. Technol. 50 (7), 3762–3772.
Wang, L., Wei, G., Li, C., Lin, A., Hu, B., Ma, Y., 2013. Measurement and estimation of photosynthetically active radiation from 1961 to 2011 in Central China. Appl. Energy 111, 1110–1117.
Wang, L., Gong, W., Xia, X., Zhu, J., Li, J., Zhu, Z., 2015. Long-term observations of aerosol optical properties at Wuhan, an urban site in Central China. Atmos. Environ. 101, 94–102.
Wang, H., Qiao, L., Lou, S., Zhou, M., Ding, A., Huang, H., Chen, J., Wang, Q., Tao, S., Chen, C., Li, L., Huang, C., 2016. Chemical composition of $PM_{2.5}$ and meteorological impact among three years in urban Shanghai, China. J. Clean. Prod. 112, 1302–1311.
WHO, 2006. WHO Air Quality Guidelines for Particulate Matter, Ozone, Nitrogen Dioxide and Sulfur Dioxide: Summary of Risk Assessment. World Health Organization, Geneva.
Wu, S., Feng, Q., Du, Y., Li, X., 2011. Artificial neural network models for daily PM_{10} air pollution index prediction in the urban area of Wuhan, China. Environ. Eng. Sci. 28, 357–363.
Wu, J., Xie, W., Li, W., Li, J., 2015. Effects of urban landscape pattern on $PM_{2.5}$ pollution—a Beijing case study. PLoS One 10 (11).
Wu, J., Yao, F., Li, W., Si, M., 2016. VIIRS-based remote sensing estimation of ground-level $PM_{2.5}$ concentrations in Beijing–Tianjin–Hebei: a spatiotemporal statistical model. Remote Sens. Environ. 184, 316–328.
Wuhan Environmental Protection Bureau (WEPB), 2016. Industrial emissions are the main source of $PM_{2.5}$. Accessible online. http://www.whepb.gov.cn/hbHjxw/19382.jhtml.
Xie, Y., Wang, Y., Zhang, K., Dong, W., Lv, B., Bai, Y., 2015. Daily estimation of ground-level $PM_{2.5}$ concentrations over Beijing using 3 km resolution MODIS AOD. Environ. Sci. Technol. 49 (20), 12280–12288.
Zhang, L., Gong, S., Padro, J., Barrie, L., 2001. A size-segregated particle dry deposition scheme for an atmospheric aerosol module. Atmos. Environ. 35 (3), 549–560.
Zhang, H., Hoff, R.M., Engel-Cox, J.A., 2009. The relation between Moderate Resolution Imaging Spectroradiometer (MODIS) aerosol optical depth and $PM_{2.5}$ over the United States: a geographical comparison by U.S. Environmental Protection Agency regions. J. Air Waste Manage. Assoc. 59, 1358–1369.
Zhang, R., Jing, J., Tao, J., Hsu, S., Wang, G., Cao, J.J., Shen, Z., 2013. Chemical characterization and source apportionment of $PM_{2.5}$ in Beijing: seasonal perspective. Atmos. Chem. Phys. 13 (14), 7053–7074.
Zhang, W., Wang, B., Niu, X., 2015. Study on the adsorption capacities for airborne particulates of landscape plants in different polluted regions in Beijing (China). Int. J. Environ. Res. Public Health 12 (8), 9623–9638.
Zhang, T., Gong, W., Wang, W., Ji, Y., Zhu, Z., Huang, Y., 2016a. Ground level $PM_{2.5}$ estimates over China using satellite-based geographically weighted regression (GWR) models are improved by including NO2and Enhanced Vegetation Index (EVI). Int. J. Environ. Res. Public Health 13, 1215.
Zhang, T., Liu, G., Zhu, Z., Gong, W., Ji, Y., Huang, Y., 2016b. Real-time estimation of satellite-derived $PM_{2.5}$ based on a semi-physical geographically weighted regression model. Int. J. Environ. Res. Public Health 13, 974. http://dx.doi.org/10.3390/ijerph13100974.
Zhang, T., Zhu, Z., Gong, W., Xiang, H., Fang, R., 2016c. Characteristics of fine particles in an urban atmosphere-relationships with meteorological parameters and trace gases. Int. J. Environ. Res. Public Health 13, 807. http://dx.doi.org/10.3390/ijerph13080807.
Zhang, T., Zhu, Z., Gong, W., Xiang, H., Li, Y., Cui, Z., 2016d. Characteristics of ultrafine particles and their relationships with meteorological factors and trace gases in Wuhan, Central China. Atmosphere 7, 96.
Zhang, G., Xu, K., Huang, W., 2017. Auto-calibration of GF-1 WFV images using flat terrain. ISPRS J. Photogramm. 134, 56–69.
Zhao, H., Che, H., Ma, Y., Xia, X., Wang, Y., Wang, P., Wu, X., 2015. Temporal variability of the visibility, particulate matter mass concentration and aerosol optical properties over an urban site in Northeast China. Atmos. Res. 166, 204–212.
Zheng, M., Cass, G.R., Schauer, J.J., Edgerton, E.S., 2002. Source apportionment of $PM_{2.5}$ in the southeastern United States using solvent-extractable organic compounds as tracers. Environ. Sci. Technol. 36 (11), 2361–2371.
Zheng, M., Salmon, L.G., Schauer, J.J., Zeng, L., Kiang, C.S., Zhang, Y., Cass, G.R., 2005. Seasonal trends in $PM_{2.5}$ source contributions in Beijing, China. Atmos. Environ. 39 (22), 3967–3976.
Zheng, B., Zhang, Q., Zhang, Y., He, K.B., Wang, K., Zheng, G.J., Duan, F.K., Ma, Y.L., Kimoto, T., 2015. Heterogeneous chemistry: a mechanism missing in current models to explain secondary inorganic aerosol formation during the January 2013 haze episode in North China. Atmos. Chem. Phys. 14, 2031–2049.
Zheng, Y., Zhang, Q., Liu, Y., Geng, G., He, K., 2016. Estimating ground-level $PM_{2.5}$ concentrations over three megalopolises in China using satellite-derived aerosol optical depth measurements. In: Proceedings from EGU General Assembly Conference.